

AgMTR: Agent Mining Transformer for Few-shot Segmentation in Remote Sensing

Hanbo Bi^{1,2,3,4} · Yingchao Feng^{1,4*} · Yongqiang Mao^{1,2,3,4,5} ·
Jianning Pei^{1,2,3,4} · Wenhui Diao^{1,4} · Hongqi Wang^{1,4} · Xian Sun^{1,2,3,4}

Received: date / Accepted: date

Abstract Few-shot Segmentation (FSS) aims to segment the interested objects in the query image with just a handful of labeled samples (i.e., support images). Previous schemes would leverage the similarity between support-query pixel pairs to construct the pixel-level semantic correlation. However, in remote sensing scenarios with extreme intra-class variations and cluttered backgrounds, such pixel-level correlations may produce tremendous mismatches, resulting in semantic ambiguity between the query foreground (FG) and background (BG) pixels. To tackle this problem, we propose a novel Agent Mining Transformer (AgMTR), which adaptively mines a set of local-aware agents to construct agent-level semantic correlation. Compared with pixel-level semantics, the given agents are equipped with local-contextual information and possess a broader receptive field. At this point, different query pixels can selectively aggregate the fine-grained local semantics of different agents, thereby enhancing the semantic clarity between query FG and BG pixels. Concretely, the Agent Learning Encoder (ALE) is first proposed to erect the optimal transport plan that arranges different agents to aggregate support semantics under different

local regions. Then, for further optimizing the agents, the Agent Aggregation Decoder (AAD) and the Semantic Alignment Decoder (SAD) are constructed to break through the limited support set for mining valuable class-specific semantics from unlabeled data sources and the query image itself, respectively. Extensive experiments on the remote sensing benchmark iSAID indicate that the proposed method achieves state-of-the-art performance. Surprisingly, our method remains quite competitive when extended to more common natural scenarios, i.e., PASCAL-5ⁱ and COCO-20ⁱ.

Keywords Few-shot Learning · Few-shot Segmentation · Remote Sensing · Semantic Segmentation

1 Introduction

Semantic segmentation (Dey et al., 2010; Diakogiannis et al., 2020; Mao et al., 2022a; Yuan et al., 2021; Feng et al., 2021), one of the fundamental tasks in the intelligent interpretation of remote sensing, aims at assigning a pre-defined target category to each pixel in remote sensing images (Wang et al., 2022a,c; Mao et al., 2023; Zhang and Zhang, 2022; Mao et al., 2024). With the recent development of deep learning techniques, especially the emergence of the fully convolutional network (FCN) (Long et al., 2015; Ronneberger et al., 2015; He et al., 2016; Chen et al., 2017), the semantic segmentation task of remote sensing has made remarkable breakthroughs. However, collecting massive pixel-level annotations for complex remote sensing scenes is time-consuming and labor-intensive (Csillik, 2017; Kotaridis and Lazaridou, 2021). Even though researchers propose weakly-supervised (Wang et al., 2020b; Schmitt et al., 2020; Lian and Huang, 2021) and semi-supervised methods (Wang et al., 2020a; Sun et al., 2020; Wang et al., 2022b; Zhang et al., 2022a) to alleviate the data hunger, they fail to effectively generalize to unseen domains. Few-shot Learning (FSL) provides a promising

Hanbo Bi (bihanbo21@mails.ucas.edu.cn)

Yingchao Feng (fengyc@aircas.ac.cn)

Yongqiang Mao (mao.yongqiang@ieee.org)

Jianning Pei (peijianning22@mails.ucas.ac.cn)

Wenhui Diao (diaowh@aircas.ac.cn)

Hongqi Wang (wieceas@sina.com)

Xian Sun (sunxian@aircas.ac.cn)

1. Aerospace Information Research Institute, Chinese Academy of Sciences

2. School of Electronic, Electrical and Communication Engineering, University of Chinese Academy of Sciences

3. University of Chinese Academy of Sciences

4. Key Laboratory of Network Information System Technology, Institute of Electronics, Chinese Academy of Sciences

5. Department of Electronic Engineering, Tsinghua University

* Corresponding authors.

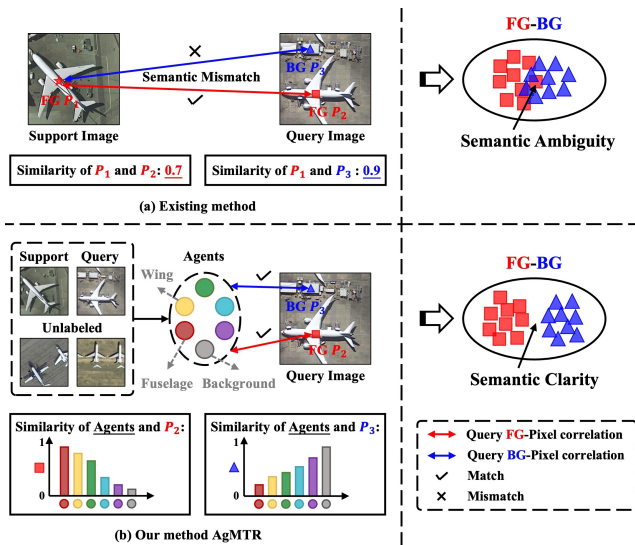


Fig. 1 (a) Due to the extreme intra-class variations and cluttered backgrounds in remote sensing scenes, directly leveraging the correlations between support-query pixel pairs to aggregate support semantics may result in tremendous mismatches. In this case, both FG and BG pixels of the query are likely to aggregate the FG semantics of the support, resulting in semantic ambiguity. (b) AgMTR mines a set of local-aware agents from support, unlabeled, and query images for constructing agent-level semantic correlation. At this point, query FG-pixel P_2 will selectively aggregate the agent semantics responsible for the 'Fuselage', while the BG-pixel P_3 will aggregate the background agent semantics, implementing semantic clarity between the query FG and BG pixels.

research solution for tackling the above issue, which can exploit several labeled samples to quickly generalize to unseen (novel) classes (Vinyals et al., 2016; Bi et al., 2023; Sung et al., 2018; Mao et al., 2022b; Wang et al., 2020c).

Few-shot Segmentation (FSS) is a natural extension of FSL for handling dense prediction tasks (Shaban et al., 2017; Zhang et al., 2019; Xu et al., 2024a,a). The purpose of FSS is to segment the corresponding object in the interested image (called query image) utilizing several labeled samples (called support images) containing the interested class. The current mainstream FSS schemes, i.e., prototype-learning and affinity-learning, are equipped with pixel-level semantic correlation in most cases. The former constructs the class-agnostic prior mask by maximizing pair-wise pixel similarity to compensate for the missing information caused by feature compression (Wang et al., 2019; Li et al., 2021; Tian et al., 2022; Lang et al., 2024), while the latter directly leverages the similarity of support-query pixel pairs to aggregate support semantics into the query feature (Zhang et al., 2021b; Wang et al., 2022d; Zhang et al., 2022c; Xu et al., 2023). For instance, CyCTR (Zhang et al., 2021b) introduced a cycle-consistent transformer to selectively aggregate support-pixel semantics and SCCAN (Xu et al., 2023) designed a self-calibrated cross-attention to alleviate the pixel-mismatch issue.

Despite the desirable results in natural scenarios, when extended to remote sensing scenarios with extreme intra-class variations and cluttered backgrounds, directly leveraging the correlations between support-query pixel pairs to aggregate support semantics may lead to tremendous mismatches. Unfortunately, the low-data regime of FSS would exacerbate these negative effects. As illustrated in Fig. 1(a), in view of the appearance difference between objects in the support-query pair and the complex background interference, the background (BG) pixel 'Roof' P_3 in the query even matches the foreground (FG) pixel 'Plane' P_1 in the support more than the FG-pixel 'Plane' P_2 in the query. At this point, both query FG and BG pixels will aggregate support FG semantics, resulting in semantic ambiguity between the FG and BG pixels of the query and yielding segmentation failures.

To correct the semantic ambiguity between the query FG and BG pixels caused by pixel-level mismatch, we suggest adaptively mining a set of local-aware agents (i.e., condensed feature representations) for constructing agent-level semantic correlation. Note that different agents will highlight different local regions of the interested class, e.g., the 'Fuselage', 'Wings', etc., of the 'Plane'. In this case, different pixels in the query image will derive the corresponding agent-level semantic correlations, thus executing specific semantic aggregations. As illustrated in Fig. 1(b), given query FG-pixel P_2 selectively aggregates the agent semantics responsible for the 'Fuselage', while the BG-pixel P_3 aggregates the background agent semantics. This is due to the fact that, compared to pixel-level semantics, the agents are equipped with local contextual information and possess a broader receptive field, thus ensuring the safe execution of semantic aggregation for query pixels and enhancing semantic clarity between query FG and BG pixels.

Nevertheless, excavating representative agents without explicit supervision is not trivial. This paper develops an Agent Mining Transformer network called AgMTR to address this issue. For minimizing the negative impact of large intra-class variations in remote sensing scenarios, besides routinely exploiting the **support images**, AgMTR focuses on exploring valuable semantics from **unlabeled images** and the **query image** itself to optimize agents. The specific process of mining agents is depicted in Fig. 2.

Firstly, the **Agent Learning Encoder (ALE)** is proposed to guide agents to efficiently mine salient semantics (i.e., class-specific semantics) from the support pixels that can help segment the target classes in the query image in a masked cross-attention manner (Cheng et al., 2022a). To enhance the semantic diversity of the agents, ALE dynamically imposes equal division constraints on the foreground region, thus assigning different yet complementary local masks to different agents. At this point, different agents can aggregate the pixel semantics from the corresponding local regions,

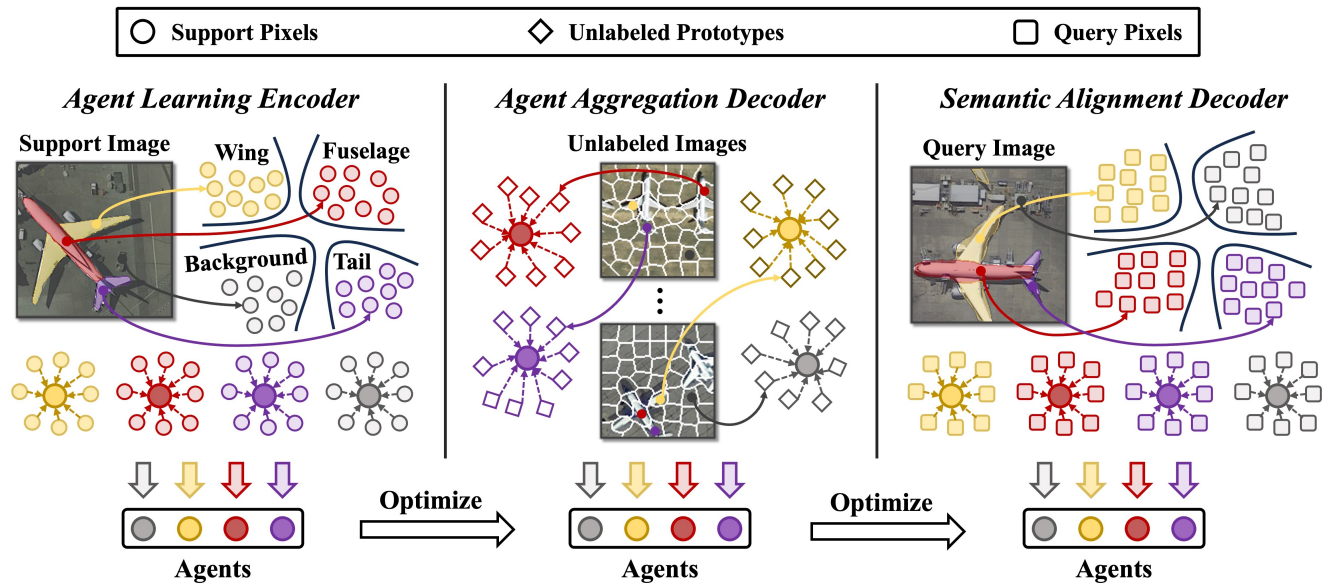


Fig. 2 The specific process of mining agents. Firstly, Agent Learning Encoder (ALE) dynamically divides the image into different but complementary local regions, e.g., ‘Fuselage’, ‘Wing’, ‘Tail’, ‘Background’, etc., via the support foreground mask, thus assigning different local semantics to different agents. To further optimize the agents, the Agent Aggregation Decoder (AAD) introduces a set of unlabeled images and obtains a set of local prototypes through unsupervised clustering, where the agents will selectively perceive and aggregate fine-grained information from these prototypes. Finally, the Semantic Alignment Decoder (SAD) constructs the query pseudo-local masks for the agents to aggregate the local semantics from the query image.

achieving the local-awareness of the target category, such as the ‘Fuselage’, and ‘Wings’ of the ‘Plane’.

Merely aggregating support semantics is not enough to bridge the semantic gap from the image pair. The **Agent Aggregation Decoder (AAD)** is proposed to introduce unlabeled images containing the interested class as references, with the expectation that agents can adaptively explore the corresponding object semantics from unlabeled data sources, thus breaking beyond the limited support set for better guiding the query segmentation. Notably, the unlabeled image features will be adaptively clustered into a set of local prototypes, where the proposed agents will selectively aggregate these prototype semantics to further enhance the local-awareness of the target category.

Furthermore, inspired by the strong intra-object similarity, i.e., pixels within the one object are more similar than pixels between different objects (Wang et al., 2024), learning from the query image itself is equally crucial to guide its own segmentation. The **Semantic Alignment Decoder (SAD)** is suggested to promote semantic consistency between the agents and the query object. Specifically, the pseudo-local masks of the query image will be constructed by computing the similarity between the different local agents and the query feature. Under the constraint of the local masks, different agents will further aggregate the corresponding query local semantics, thus aligning with the query semantics.

Based on the above three components, AgMTR constructs precise agent-level semantic correlations, effectively

distinguishing FG and BG pixels in the semantic aggregation of the query feature.

The primary contributions can be summarized as follows:

- A novel Agent Mining Transformer (AgMTR) network for FSS in remote sensing is proposed to adaptively mine a set of local-aware agents for different objects to construct agent-level semantic correlation, thus correcting the semantic ambiguity between the query FG and BG pixels caused by pixel-level mismatches.
- We construct an Agent Learning Encoder, Agent Aggregation Decoder, and Semantic Alignment Decoder to adaptively mine and optimize agent semantics from support, unlabeled, and query images, in that order.
- Extensive experiments on remote sensing FSS benchmark iSAID, validate the superiority of the proposed AgMTR and achieve state-of-the-art performance. Surprisingly, our method likewise outperforms previous SOTA on two popular CV benchmarks, PASCAL-5ⁱ, and COCO-20ⁱ.

2 Related work

2.1 Semantic Segmentation

Semantic segmentation, with the goal of predicting pixel-level labels within an image, has been widely emphasized by researchers as a fundamental task in image interpretation. Long et al. (Long et al., 2015) first proposed a full convolutional network (FCN) for the semantic segmentation task,

providing a solid foundation for the following research. To further mine the association of contextual information, Chen et al. (Chen et al., 2014) proposed Dilated Convolution to expand the convolutional receptive field. Meanwhile, Zhao et al. (Zhao et al., 2017) and Chen et al. (Chen et al., 2017) proposed Pyramid Pooling Module (PPM) and Atrous Spatial Pyramid Pooling (ASPP), respectively, to combine the feature representations between different scales and regions for multi-scale semantic aggregation.

On this basis, some researchers have focused on designing semantic segmentation methods specific to remote sensing scenes. Feng et al. (Feng et al., 2020) proposed a neighboring pixel affinity loss (NPALoss) to focus on the optimization for small-size objects and hard object boundaries. Peng et al. (Peng et al., 2021) proposed a Cross Fusion Network (CF-Net) for fast and effective extraction of small-scale objects. In addition, Niu et al. (Niu et al., 2022) decoupled the semantic segmentation task and proposed a disentangled learning paradigm to model foreground and boundary objects separately. Despite promising success with large-scale data, these methods fail to perform well when generalizing to unseen domains.

2.2 Few-shot Learning

Recently community researchers have proposed Few-shot Learning (FSL) (Xu et al., 2024b; Finn et al., 2017; Jamal and Qi, 2019; Snell et al., 2017) for fast generalization to unseen classes, which aims to recognize novel (unseen) classes from a handful of labeled samples (Wang et al., 2020c). In general, FSL methods would employ the meta-learning paradigm (Finn et al., 2017), where the model understands representative knowledge from the training dataset (seen classes) and generalizes it to novel tasks (unseen classes). On this basis, these methods can be divided into the following two branches: (i) Optimization-based method (Finn et al., 2017; Li et al., 2017; Jamal and Qi, 2019; Sun et al., 2019), which aims to search for a set of proper parameters for the model that can be easily generalized to various novel tasks. For example, Finn et al. (Finn et al., 2017) learned the initialization parameters of the model while Ravi et al. (Ravi and Larochelle, 2016) learned an optimization strategy instead of a fixed optimizer to facilitate faster convergence. (ii) Metric-based method (Vinyals et al., 2016; Snell et al., 2017; Sung et al., 2018; Ye et al., 2020; Zhang et al., 2022b), which aims to find a specific embedding space that can efficiently distinguish different classes for classification. For example, Zhang et al. (Zhang et al., 2022b) utilized Earth Mover’s Distance (EMD) to model the distance between images as the optimal transport plan. Bateni et al. (Bateni et al., 2020) proposed to construct Mahalanobis-distance classifiers to improve the accuracy of few-shot classification.

In addition, given the large intra-class variations and small inter-class variations of remote sensing scenarios, some FSL methods specific to remote sensing scenarios have been successively proposed (Alajaji et al., 2020; Zhong et al., 2020; Cheng et al., 2021; Kim and Chi, 2021; Zhu et al., 2023). In this paper, we instead apply FSL to the more advanced task of scene understanding rather than scene classification in remote sensing scenes, i.e., semantic segmentation.

2.3 Few-shot Segmentation

Few-shot Segmentation (FSS) (Wang et al., 2019; Zhang et al., 2019; Bi et al., 2024; Liu et al., 2022a; Zhang et al., 2021a), a natural extension of Few-shot Learning to tackle intensive prediction tasks, is proposed to guide the model to activate corresponding objects in the query image utilizing several labeled samples (i.e., support images) containing the interested class. Current FSS methods can be broadly divided into two parts: (i) Prototype-learning, which aims to compress the support feature into a prototype through masked average pooling (MAP), and perform feature comparison with the query feature to segment the interested object (Wang et al., 2019; Zhang et al., 2019; Liu et al., 2022a; Zhang et al., 2021a). However, these methods would inevitably lose spatial information and lack context-awareness. To address this issue, besides attempting to generate multiple prototypes (Liu et al., 2020b; Yang et al., 2020a), they typically constructed the class-agnostic prior mask by maximizing pair-wise pixel similarity to further mine pixel-level support semantics (Wang et al., 2019; Li et al., 2021; Tian et al., 2022; Lang et al., 2024). (ii) Affinity-learning (Zhang et al., 2021b; Wang et al., 2022d; Zhang et al., 2022c; Xu et al., 2023), which aims to directly construct pixel-level feature matching for segmentation. For instance, Zhang et al. (Zhang et al., 2021b) introduced a cycle-consistent transformer to aggregate support-pixels semantics selectively. Xu et al. (Xu et al., 2023) designed a self-calibrated cross-attention to alleviate the pixel-mismatch issue. However, such pixel-level similarity would ignore contextual information and tend to be affected by background clutter or noisy pixels causing semantic ambiguity. We propose feature embeddings called agents, which are condensed feature representations similar to prototypes, and at the same time mine the valuable pixel semantics for dynamic optimization, which can combine the strengths of prototype learning and affinity learning.

In addition, several methods, such as BAM (Lang et al., 2023c), D²Zero (He et al., 2023b), and PADing (He et al., 2023a), focus on addressing the bias toward seen classes in Few-shot (Zero-shot) scenes for better generalize to unseen classes. In the field of remote sensing, the Few-shot Segmentation task has also received an enthusiastic response (Yao et al., 2021; Wang et al., 2021; Jiang et al., 2022; Lang et al., 2023b,e; Bi et al., 2023). Yao et al. (Yao et al., 2021) proposed

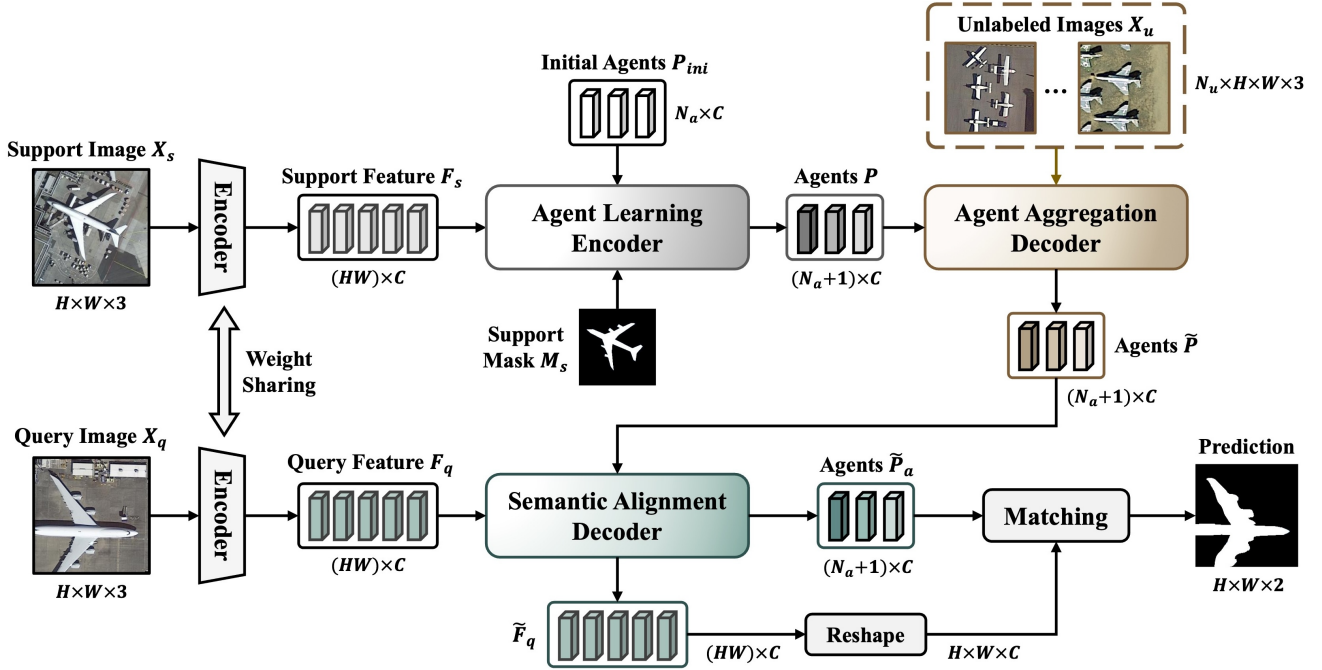


Fig. 3 The overall pipeline of the proposed AgMTR, aims at constructing agent-level semantic correlation to correct the semantic ambiguity between the query FG and BG pixels caused by pixel-level mismatches. Three components are proposed to excavate representative agents without explicit supervision: Agent Learning Encoder (ALE), Agent Aggregation Decoder (AAD), and Semantic Alignment Decoder (SAD). First, ALE dynamically divides the support mask into multiple local masks, thus guiding different agents to mine the semantics under different local masks for local-awareness. AAD then introduces a series of unlabeled images where the agents could selectively perceive and aggregate semantics beneficial to them from the unlabeled data source to break through the limited support set. Finally, SAD aims to mine the query image’s own interested semantics to promote semantic consistency between the agents and the query object.

a scale-aware prototype matching scheme to handle the large variance of objects’ appearances and scales. Bi et al. (Bi et al., 2023) designed DMNet to mine the class-specific semantics from query images. To maximize the breakthrough of the few-shot limitations for better adapting to remote sensing scenarios, this paper proposes to mine and optimize class-specific semantics from support, unlabeled, and query images.

3 Problem Definition

The purpose of Few-shot Segmentation (FSS) is to segment unseen class objects without additional training by utilizing only a handful of labeled samples. Following the mainstream schemes (Bi et al., 2023; Lang et al., 2024), the meta-learning paradigm is employed to train the model. Concretely, given a training dataset D_{train} with seen classes C_{seen} and a testing dataset D_{test} with unseen classes C_{unseen} ($C_{seen} \cap C_{unseen} = \emptyset$), the model would understand representative knowledge from multiple tasks (i.e., episodes) sampled from D_{train} , and then generalizes directly to D_{test} . Specifically, both datasets D_{train} and D_{test} consist of multiple episodes, each containing a support set $S = \{(X_s^i, M_s^i)\}_{i=1}^K$ and a query set $Q = \{(X_q, M_q)\}$, where X_s^i and M_s^i denote the image and the corresponding mask containing the interested class, respectively, K denotes the number of support image

provided in S . During each training episode, the FSS models are optimized by predicting the query image X_q with the guidance of the support set S . After training, the model evaluates the performance in each testing episode on D_{test} without any optimization. Note that the query mask M_q is not available during the testing phase.

Variant: Considering that extreme intra-class variations in remote sensing scenarios would further exacerbate the gap between support-query image pairs in FSS, it is sub-optimal and insufficient for previous work to utilize only support images (i.e., labeled samples) to guide the query image. Thus, this paper also introduces unlabeled sample set $S_u = \{(X_u^i)\}_{i=1}^{N_u}$ with the same interested class as the labeled samples to assist in segmentation. These samples are derived by random sampling from the interested class during the training and testing phase, with the corresponding masks removed. At this point, the model will segment the image X_q with the guidance of S and S_u .

4 Proposed Method

4.1 Method Overview

To correct the semantic ambiguity of query FG and BG pixels caused by the semantic mismatch in previous pixel-level

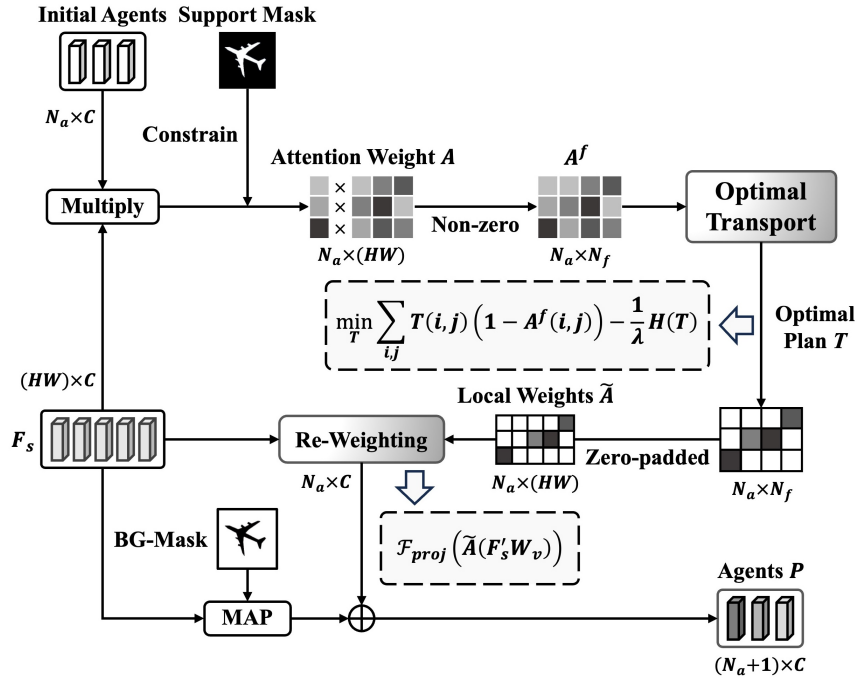


Fig. 4 The detailed pipeline of Agent Learning Encoder (ALE), which aims at driving the agents to efficiently capture interested information from support pixels through the masked cross-attention mechanism. To enhance the semantic diversity of agents, ALE dynamically decomposes the foreground mask into different yet complementary local masks, thus ensuring that different agents aggregate different local semantics.

semantic correlation, this paper develops an Agent Mining Transformer network named AgMTR, which suggests mining a set of local-aware agents (i.e., condensed feature representations similar to prototypes), and relies on them to construct agent-level semantic correlation. Across tasks, the proposed agents are not static, or an agent contains the local semantics of multiple classes. On the contrary, the semantic awareness of the agents is dynamic, where AgMTR would adaptively mine the corresponding class-specific semantics according to the target classes of different episodes/tasks, thus generating local-aware agents for the current class. Compared to prototypes, agents offer more precise and stable feature representations, a richer and more diverse semantic source, and enhanced local contextual awareness.

The overall pipeline is depicted in Fig.3. In particular, given the support-query image pair X_s and X_q , we extract features with a shared-feature encoder (e.g., ViT (Dosovitskiy et al., 2020) and DeiT (Touvron et al., 2021)) to derive the support feature $F_s \in \mathbb{R}^{H \times W \times C}$ and query feature $F_q \in \mathbb{R}^{H \times W \times C}$. For more matched agent-level semantic correlation, AgMTR constructs three components, Agent Learning Encoder (ALE), Agent Aggregation Decoder (AAD), and Semantic Alignment Decoder (SAD), to dynamically mine and optimize agent semantics from support, unlabeled, and query images, in that order:

- **Agent Learning Encoder:** ALE dynamically decomposes the support mask into multiple local masks and arranges different initial agents to aggregate the support

semantics under different local masks for deriving local-awareness of the target category.

- **Agent Aggregation Decoder:** To break through the limited support set for better guidance, AAD introduces unlabeled images containing the interested class, where the agents will selectively perceive and aggregate the semantics beneficial to them from unlabeled images.
- **Semantic Alignment Decoder:** To further bridge the semantic gap, SAD constructs the pseudo-local masks of the query image, which drives the agents to aggregate the local semantics of the query itself to promote semantic consistency with the query object.

4.2 Agent Learning Encoder

As mentioned in Sec.1, we suggest mining a set of context-rich agents to perform agent-level semantic correlation replacing the previous pixel-level. At this point, the focus turns to capturing representative agents. Agent Learning Encoder aims to guide agents to efficiently mine salient semantics (i.e., class-specific semantics) from the support pixels that can help segment the target classes in the query image, which is the most basic and important step, with the detailed pipeline illustrated in Algorithm 1.

Agent Initialization: Firstly, as depicted in Fig.4, the initial agents $P^{ini} = [p_1^{ini}, p_2^{ini}, \dots, p_{N_a}^{ini}] \in \mathbb{R}^{N_a \times C}$ are derived by adding between randomly initialized feature embeddings

Algorithm 1: Agent Learning Encoder (ALE)

-
- Input:** Support feature F_s , Support mask M_s
Output: Local-aware agents P
- 1 **Step 1: Agent Initialization**
 - 2 Generate initial agents $P^{ini} \leftarrow (F_s, M_s)$ according to Eq.(1);
 - 3 **Step 2: Agent Learning**
 - 4 Construct attention weight between agents and the feature $A \leftarrow (P^{ini}, F_s, M_s)$ according to Eq.(2)-Eq.(3);
 - 5 Decompose the attention weight A into different but complementary local attention weights \tilde{A} according to Eq.(4)-Eq.(5);
 - 6 Generate corresponding local agent based on different local attention weights $P \leftarrow (\tilde{A}, F_s)$ according to Eq.(6);
-

$\{t_i\}_1^{N_a} \in \mathbb{R}^{N_a \times C}$ and the support prototype obtained by performing masked average pooling (MAP) operation:

$$p_i^{ini} = \text{MAP}(F_s \odot M_s) + t_i, i = 1, 2, \dots, N_a \quad (1)$$

where $\text{MAP}(\cdot)$ denotes the compression of the support feature F_s under the foreground mask M_s into a feature vector and \odot denotes the dot product. Notably, the randomly initialized feature embeddings $\{t_i\}_1^{N_a}$ obeys a normal distribution. **Agent Learning:** To empower agents with context-awareness, ALE employs masked cross-attention (Cheng et al., 2022a) to aggregate the interested semantics in the support feature to corresponding agents. At this point, the attention weight $A \in \mathbb{R}^{N_a \times HW}$ between agents and feature can be formulated as:

$$A = \text{softmax} \left(\frac{(P^{ini} W_q) (F'_s W_k)^T}{\sqrt{d}} + \tilde{M}_s \right) \quad (2)$$

where $W_* \in \mathbb{R}^{C \times C}$ denote projection weights, $F'_s \in \mathbb{R}^{HW \times C}$ denotes the flattened support feature. Notably, we utilize \tilde{M}_s to constrain the region of interest for the attention weight:

$$\tilde{M}_s(i) = \begin{cases} 0, & \text{if } M'_s(i) = 1 \\ -\infty, & \text{otherwise} \end{cases} \quad (3)$$

where M'_s denotes the flattened support mask. After normalization in Eq.(2), the attention weight A focuses only on the foreground region of the support mask, thus ensuring that the agents aggregate only the interested foreground semantics.

Without supervising the learning process, such agents tend to capture similar foreground semantics resulting in redundancy. To enhance the semantic diversity of agents, we propose decomposing the attention weight into different but complementary local attention weights, i.e., decomposing the support mask into different local masks. Under the constraint of those local masks, different agents can aggregate

the semantics from different local regions, yielding different local perceptions of the target category.

Concretely, we model this allocation as the Optimal Transport (OT) problem. By searching for the transport plan with the minimum transport cost, the pixel allocation of different agents is accomplished, which can be solved efficiently by the Sinkhorn (Cuturi, 2013) algorithm. We define the cost matrix as $(1 - A^f)$, where $A^f \in \mathbb{R}^{N_a \times N_f}$ denotes the similarity matrix between the agents and the foreground feature of the support image instead of the whole feature. Notably, the larger $A^f(i, j)$ is, the greater the similarity between the i^{th} agent and the j^{th} support pixel, the lower the transport cost, and the greater the likelihood that the pixel will be assigned to that agent. At this point, the transport plan is denoted as $T \in \mathbb{R}^{N_a \times N_f}$, with the optimization function formulated as:

$$\min_{T \in \mathcal{Y}} \sum_{i,j} T(i, j) (1 - A^f(i, j)) - \frac{1}{\lambda} H(T) \quad (4)$$

where $H(T) = -\sum_{i,j} T(i, j) \log T(i, j)$ denotes entropy regularization and λ is responsible for adjusting the degree of entropy impact. Besides, the transport plan T needs to obey the distribution of \mathcal{Y} :

$$\mathcal{Y} = \left\{ T \in \mathbb{R}^{N_a \times N_f} \mid T \mathbf{I}_m = \frac{1}{N_a} \mathbf{I}_n, T^T \mathbf{I}_n = \frac{1}{N_f} \mathbf{I}_m \right\} \quad (5)$$

where $\mathbf{I}_m \in \mathbb{R}^{N_f}$ and $\mathbf{I}_n \in \mathbb{R}^{N_a}$ denote vectors with values of 1 in all dimensions. Eq.(5) aims to force each agent to allocate the same number of foreground pixels, avoiding a situation where all pixels are allocated to one agent.

After deriving the optimal transport plan T , we zero-padded it to recover the background region to produce the local attention weights $\tilde{A} \in \mathbb{R}^{N_a \times HW}$. At this point, different agents P will aggregate the corresponding pixel semantics under the constraint of local weights:

$$P = \mathcal{F}_{proj} \left(\tilde{A} (F'_s W_v) \right) \quad (6)$$

where \mathcal{F}_{proj} denotes the two-layer MLP and W_v denotes the projection weight.

Note that the agents are not the multiple local regions divided by the ALE, but rather the product of condensing the pixel semantics of different local regions into a single feature vector. Finally, the background prototype derived by performing MAP on the support feature will be incorporated as the background agent in $P = [p_1, p_2, \dots, p_{N_a}, p_{N_a+1}] \in \mathbb{R}^{(N_a+1) \times C}$.

4.3 Agent Aggregation Decoder

Capturing the class-specific semantics from the support images merely is not sufficient to bridge the semantic gap between the image pairs, especially in complex remote sensing scenarios. To break through the limited support set for

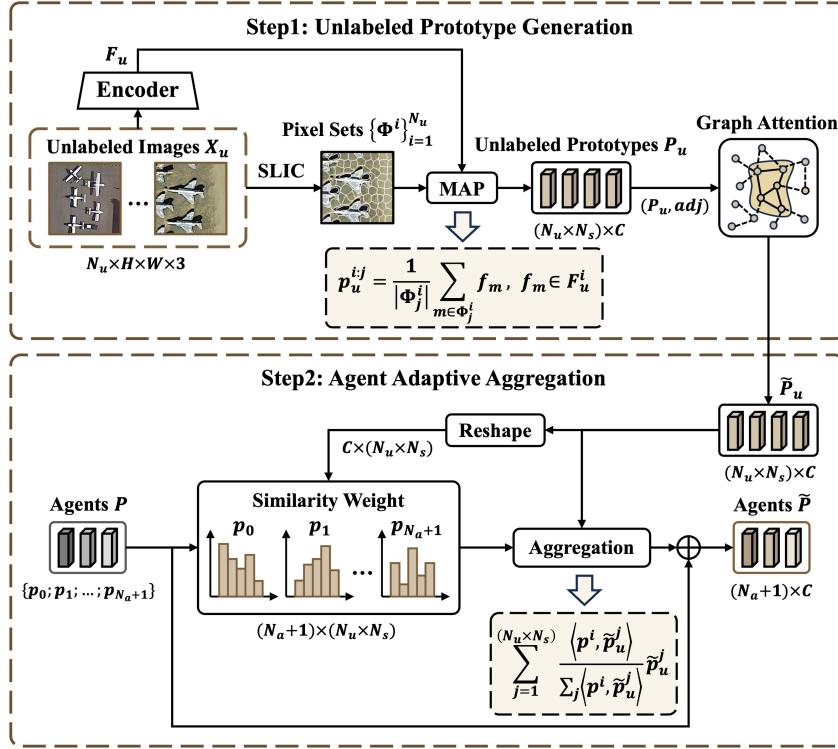


Fig. 5 The detailed pipeline of Agent Aggregation Decoder (AAD). AAD introduces unlabeled images containing the interested class as a reference, expecting agents to adaptively explore the richer interested semantics from unlabeled data sources to break through the support set limitations.

Algorithm 2: Agent Aggregation Decoder (AAD)

Input: Local agents P , Unlabeled sample set S_u

Output: Refined local agents \tilde{P}

1 Step 1: Unlabeled prototype generation

- 2 First, generate unlabeled features $F_u \leftarrow S_u$;
- 3 Obtain a series of pixel sets by clustering and compress them into local prototypes $P_u \leftarrow F_u$ according to Eq.(7);
- 4 Enhance the contextual semantics of the unlabeled prototypes $\tilde{P}_u \leftarrow P_u$ according to Eq.(8);

5 Step 2: Agent Adaptive Aggregation

- 6 Different agents adaptively aggregate the beneficial semantics for them from unlabeled prototypes $\tilde{P} \leftarrow (P, \tilde{P}_u)$ according to Eq.(9);
-

mitigating the intra-class variations, the Agent Aggregation Decoder introduces unlabeled images containing the interested class as a reference, expecting agents to adaptively explore the richer interested semantics from the unlabeled data source, with the pipeline illustrated in Algorithm 2.

Unlabeled prototype generation: Specifically, as illustrated in Fig.5, given N_u unlabeled images X_u , we extract features via a shared encoder to generate unlabeled features $F_u \in \mathbb{R}^{N_u \times H \times W \times C}$. Considering that there is a significant amount of background noise in the unlabeled feature that cannot be directly exploited, we employ a super-pixel scheme SLIC (Achanta et al., 2012) to cluster the unlabeled image

into N_s pixel sets $\Phi^i = \{\Phi_1^i, \Phi_2^i, \dots, \Phi_{N_s}^i\}, i = 1, 2, \dots, N_u$ based on color, texture, and distance. The unlabeled features can be compressed into a series of local prototypes $P_u \in \mathbb{R}^{(N_u \times N_s) \times C}$ through MAP operation:

$$p_u^{i,j} = \frac{1}{|\Phi_j^i|} \sum_{m \in \Phi_j^i} f_m, f_m \in F_u^i \quad (7)$$

where $p_u^{i,j} \in \mathbb{R}^C$ denotes the j^{th} local prototype generated by the i^{th} unlabeled image and Φ_j^i denotes the j^{th} pixel set generated by the i^{th} unlabeled image.

To further enhance the contextual semantics of the unlabeled prototype set, we model it as the graph, with the prototypes considered as nodes in the graph, employing a graph attention network (GAT) (Veličković et al., 2017) to enhance the semantic associations between nodes, which can be formulated as:

$$\begin{aligned} \tilde{P}_u &= \text{GAT}(P_u, adj) \\ \text{s.t. } adj(m, n) &= \begin{cases} 1, & \text{if } \langle p_u^m, p_u^n \rangle > \delta \\ 0, & \text{otherwise} \end{cases} \end{aligned} \quad (8)$$

where GAT denotes the graph attention network, $adj \in \mathbb{R}^{(N_u \times N_s) \times (N_u \times N_s)}$ denotes the adjacency matrix formed between the nodes and $\langle \cdot, \cdot \rangle$ denotes the cosine similarity function, $p_u^* \in \mathbb{R}^C$ denotes the $*^{th}$ prototype in the unlabeled prototype set, and δ is a threshold to determine whether

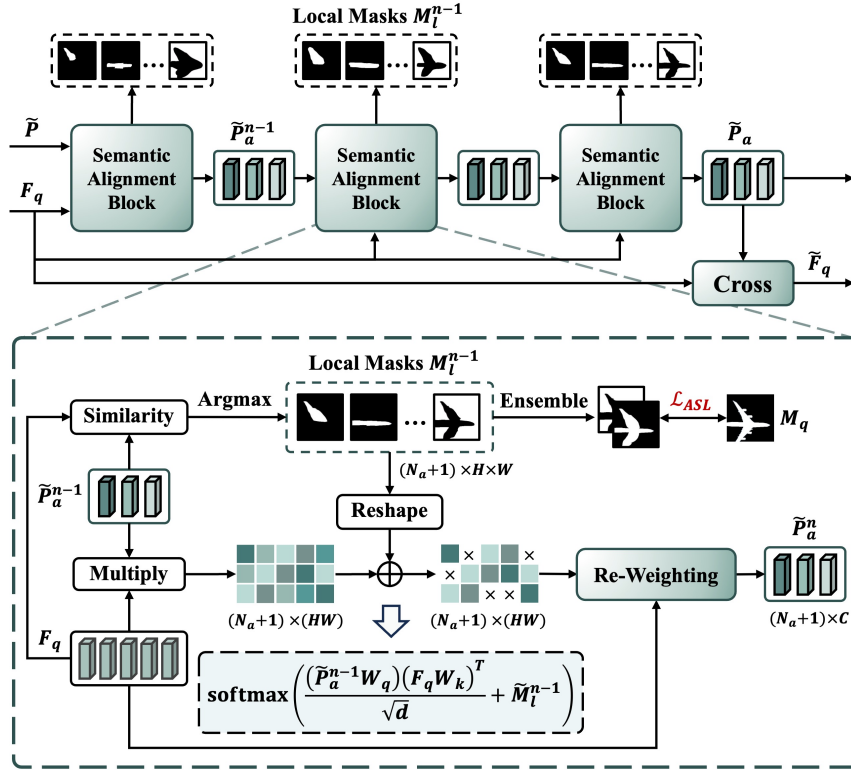


Fig. 6 The detailed pipeline of Semantic Alignment Decoder (SAD), which consists of multiple Semantic Alignment Blocks (SABs). For further aligning with the query object to bridge the semantic gap, SAB constructs the pseudo-local mask of the query image, which drives the agents to mine the local semantics of the query itself. Notably, We iterate the SAB process multiple times to gradually improve the quality of the pseudo-local mask, further promoting semantic consistency between the agents and the query object. \tilde{M}_l in the figure denotes the attention weight derived from the mapping the local mask M_l through Eq.(3).

the nodes are neighboring or not, which is set to 0.5 in the experiments.

Agent Adaptive Aggregation: Given the augmented prototypes of unlabeled features $\tilde{P}_u \in \mathbb{R}^{(N_u \times N_s) \times C}$, the agents $P \in \mathbb{R}^{(N_a+1) \times C}$ will selectively perceive and aggregate object semantics from these prototypes that are beneficial to them in a cross-attention manner. As depicted in Fig.5, by performing similarity computation with unlabeled prototypes \tilde{P}_u , different agents P will receive different similarity weights, resulting in different weighted semantic aggregations:

$$\tilde{p}^i = p^i + \beta \sum_{j=1}^{(N_u \times N_s)} \frac{\langle p^i, \tilde{p}_u^j \rangle}{\sum_j \langle p^i, \tilde{p}_u^j \rangle} \tilde{p}_u^j \quad (9)$$

where β denotes the learnable weight to balance the semantic aggregation, which is initialized to 0.4. At this point, the local agents $\tilde{P} \in \mathbb{R}^{(N_a+1) \times C}$ will be further optimized.

4.4 Semantic Alignment Decoder

Based on the observation of strong intra-object similarity, i.e., pixels within the one object are more similar than pixels

Algorithm 3: Semantic Alignment Decoder (SAD)

Input: Local agents \tilde{P} , Query feature F_q

Output: Aligned agents \tilde{P}_a , Aligned query feature \tilde{F}_q

- 1 **for** i in N **do**
- 2 **Step 1 : Semantic Alignment Block**
- 3 Construct pseudo-local masks for the query image with local agents $M_l \leftarrow (\tilde{P}, F_q)$ according to Eq.(10);
- 4 Different agents selectively aggregate query semantics under corresponding local masks $\tilde{P}_a \leftarrow (\tilde{P}, F_q, M_l)$ according to Eq.(11);
- 5 **end**
- 6 **Step 2:** The query feature aggregates the agents' semantics to enable semantic alignment $\tilde{F}_q \leftarrow (F_q, \tilde{P}_a)$.

between different objects (Wang et al., 2024), we argue that it is also crucial to mine the valuable information from the query image itself, which has been omitted in previous work. Thus, the Semantic Alignment Decoder is proposed to drive the agents to mine the class-specific semantics from the query image for promoting semantic consistency with the query object, with the pipeline illustrated in Algorithm 3.

Semantic Alignment Block: Concretely, as depicted in Fig.6, SAD consists of multiple Semantic Alignment Blocks

(SABs) in series, each of which continuously aggregates the query semantics for agents via the cross-attention. We construct the pseudo-local masks of the query image to force different agents to selectively aggregate their desired local semantics without introducing irrelevant noise. More specifically, we perform similarity computation of query feature F_q with different agents \tilde{p}^* to produce multiple segmentation results y_l^* , based on which we can gain the agent index corresponding to the maximum value of each position. Finally, the binary local masks $M_l \in \mathbb{R}^{(N_a+1) \times H \times W}$ corresponding to different agents can be derived by one-hot coding. The above process can be formulated as:

$$M_l = \text{OneHot} \left(\arg \max_i \left(\bigcup_{i=1}^{N_a+1} y_l^i \right) \right) \quad (10)$$

s.t. $y_l^i = \langle F_q, \tilde{p}^i \rangle$

where $\text{OneHot}(\cdot)$ denotes the process of encoding the local mask into binary masks, \bigcup denotes the concatenation of multiple segmentation results, and $\arg \max$ denotes the process of deriving the index corresponding to the maximum value at each pixel position.

Under the constraint of these local masks $M_l = [m_l^1, m_l^2, \dots, m_l^{(N_a+1)}]$, different agents could selectively aggregate the local semantics within their respective corresponding masks in the query image without creating semantic confusion among agents. The above process can be formulated as:

$$\tilde{p}_a^i = \text{softmax} \left(\frac{(\tilde{p}^i W_q) (F_q W_k)^T}{\sqrt{d}} + \tilde{m}_l^i \right) (F_q W_v) \quad (11)$$

where $\tilde{P}_a = [\tilde{p}_a^1, \tilde{p}_a^2, \dots, \tilde{p}_a^{(N_a+1)}]$ denote the aligned agents, \tilde{p}^i denotes the i^{th} agent, F_q denotes the query feature, \tilde{m}_l^i denotes the attention weight derived from the mapping the i^{th} local mask m_l^i through Eq.(3), and W_* denote the projection weights. Notably, the two-layer MLP in the semantic aggregation is omitted to simplify the formulation.

Multiple block iterations: Since the Semantic Alignment Block can drive agents to aggregate the corresponding local semantics in the query image to align with the query object. We can iterate the process multiple times to gradually improve the quality of the pseudo-local mask, thus further promoting semantic consistency between the agents and the query object. Suppose we have N -layer Semantic Alignment Blocks, then for each layer n :

$$\tilde{P}_a^n, M_l^{n-1} = \text{SAB} \left(\tilde{P}_a^{n-1}, F_q \right), n = 1, 2, 3, \dots, N \quad (12)$$

where SAB denotes the Semantic Alignment Block. Notably, after generating the last-layer aligned agents \tilde{P}_a , we construct cross-attention to drive the query feature \tilde{F}_q to aggregate the agents' semantics, thus enabling semantic alignment.

Agent Segmentation Loss: To supervise that each Semantic Alignment Block works, we construct an Agent Segmentation Loss for constraint. Specifically, we ensemble the local segmentation results $\{y_l^i\}_{i=1}^{N_a+1}$ received from each SAB to derive foreground-background binary prediction result, i.e., $\left[y_l^{(N_a+1)}; \max_i \left(\bigcup_{i=1}^{N_a} y_l^i \right) \right]$, where $y_l^{(N_a+1)}$ denotes the segmentation result from the background agent while other y_l^i denote the segmentation result from other foreground agents. Here, we utilize binary cross-entropy (BCE) to constrain the prediction:

$$\mathcal{L}_{ASL} = \text{BCE} \left(\left[y_l^{(N_a+1)}; \max_i \left(\bigcup_{i=1}^{N_a} y_l^i \right) \right], M_q \right) \quad (13)$$

Thus, with N -layer Semantic Alignment Blocks, N losses are produced, where we take the mean as the final loss \mathcal{L}_{ASL} .

4.5 Matching

Given the final aligned agents $\tilde{P}_a \in \mathbb{R}^{(N_a+1) \times C}$ and the aligned query feature $\tilde{F}_q \in \mathbb{R}^{H \times W \times C}$, the segmentation result $\mathcal{P} \in \mathbb{R}^{H \times W \times 2}$ can be achieved by performing similarity computation between \tilde{F}_q and the agents \tilde{P}_a (including foreground agents $\{\tilde{p}_a^i\}_{i=1}^{N_a}$ and the background agent $\tilde{p}_a^{N_a+1}$), which can be formulated as:

$$\mathcal{P} = \left[\langle \tilde{F}_q, \tilde{P}_a^{N_a+1} \rangle; \max_i \left(\bigcup_{i=1}^{N_a} \langle \tilde{F}_q, \tilde{P}_a^i \rangle \right) \right] \quad (14)$$

where $\langle \cdot, \cdot \rangle$ denotes the similarity computation and \bigcup denotes the concatenation of multiple segmentation results. Notably, the maximum operation $\max(\cdot)$ allows finding the foreground local agent that best matches the query pixel, thus effectively utilizing the local semantics to distinguish between the FG and BG pixels of the query image.

In this case, the binary cross entropy (BCE) loss \mathcal{L}_{main} is employed to supervise the optimization of the segmentation prediction \mathcal{P} towards M_q . Thus, the total loss \mathcal{L} of the model consists of \mathcal{L}_{main} and \mathcal{L}_{ASL} :

$$\mathcal{L} = \mathcal{L}_{main} + \gamma \mathcal{L}_{ASL} \quad (15)$$

where γ aims to balance the contributions of \mathcal{L}_{main} and \mathcal{L}_{ASL} .

5 Experiments

Firstly, Sec.5.1 describes the experimental setup, including dataset introduction, implementation details, and evaluation metrics. Then, Sec.5.2 and Sec.5.3 conduct extensive comparative experiments and ablation studies to prove the superiority of our method, respectively. Finally, Sec.5.6 provides several failure cases.

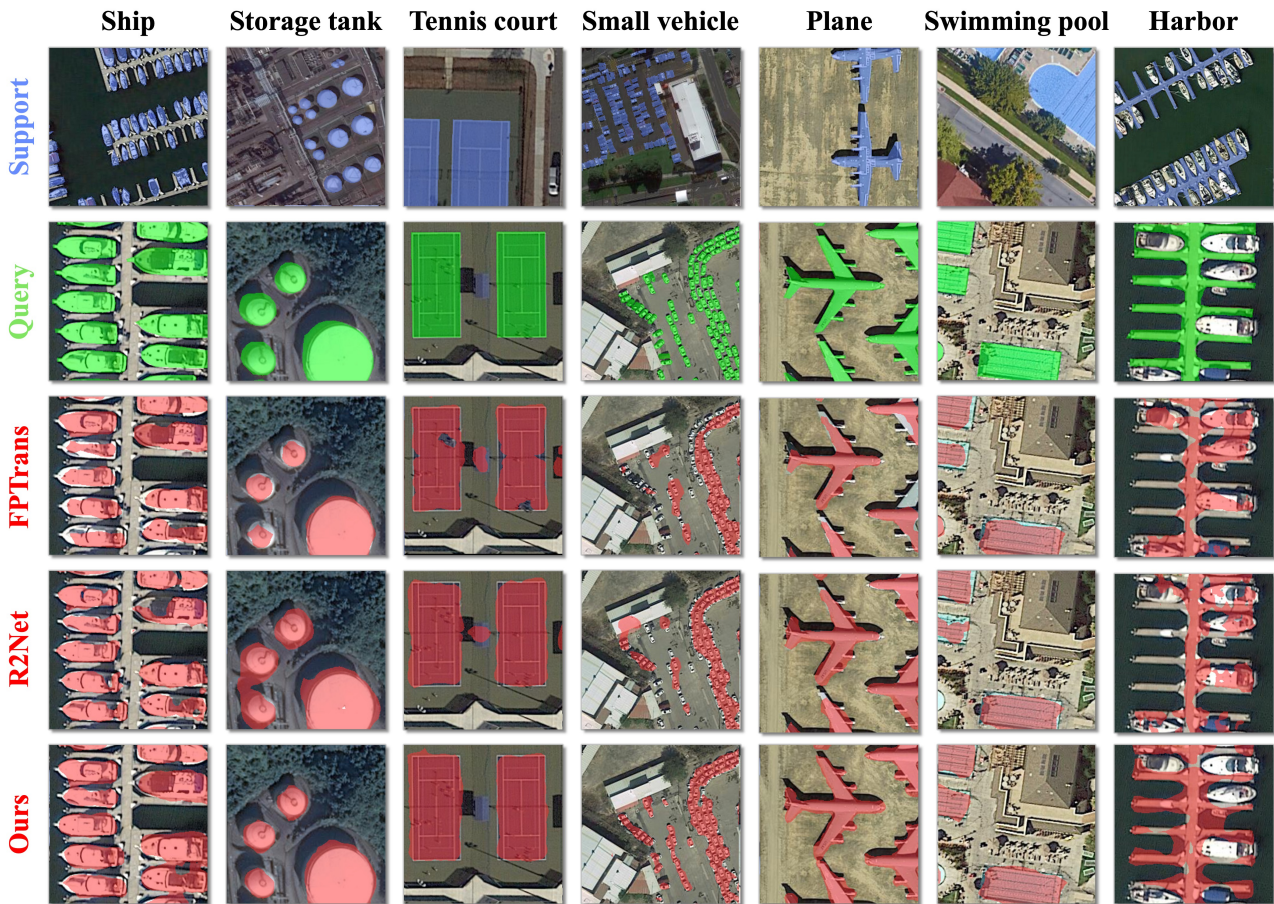


Fig. 7 Qualitative visualization of our AgMTR and several competing methods under the 1-shot setting on iSAID benchmark. From top to bottom, each row represents: support images with GT (blue), query images with GT (green), segmentation results of FPTrans (red), segmentation results of R2Net (red), and our segmentation results (red).

5.1 Experimental Setup

5.1.1 Datasets

Three FSS benchmarks are utilized for evaluation, including a remote sensing benchmark iSAID (Bi et al., 2023) and two CV benchmarks PASCAL-5ⁱ (Lang et al., 2023d) and COCO-20ⁱ (Tian et al., 2022).

iSAID (Waqas Zamir et al., 2019), a massive benchmark for intensive prediction tasks in remote sensing scenarios, contains 655,451 objects from 15 classes in 2,806 high-resolution images. Following the setup of DMNet (Bi et al., 2023), this dataset can be utilized for evaluating the FSS task. Concretely, the 15 classes will be split into three folds, each containing 10 training classes and 5 testing classes. Remarkably, both training and testing classes are disjointed in each fold to build unseen class situations. For each fold, we randomly sample 1000 image pairs for validation.

PASCAL-5ⁱ, which is constructed from PASCAL VOC 2012 (Everingham et al., 2010) and additional SBD (Har-
iharan et al., 2014), contains 20 classes in total. For cross-

validation, these classes will be split into four folds, each containing 15 training classes and 5 testing classes as done in OSLSM (Shaban et al., 2017). For each fold, we randomly sample 5000 image pairs for validation.

COCO-20ⁱ, which is constructed from MS COCO (Lin et al., 2014), contains 80 classes in total. For cross-validation, these classes will be split into four folds, each containing 60 training classes and 20 testing classes as done in (Lang et al., 2024). For each fold, we randomly sample 5000 image pairs for validation.

5.1.2 Implementation Details

The model¹ is implemented on Tesla A40 GPUs using the PyTorch framework (Paszke et al., 2019). The SGD optimizer is utilized to optimize the model during the training phase, with the weight decay set to 0.00005. The batch size is set to 8 and the initial learning rate is set to 0.002, where the poly strategy (Chen et al., 2017) is utilized to adjust the learning rate. For iSAID, we resize the images to 256×256 and set 40

¹ The codes are available at <https://github.com/HanboBiz/AgMTR/>.

Table 1 Performance comparison on iSAID benchmark measured in mIoU and FB-IoU(%) under the 1- and 5-shot settings. The ‘Mean’ and ‘FB-IoU’ indicate the averaged mIoU accuracy and the averaged FB-IoU accuracy for all classes under all folds, respectively.

Backbone	Method	1-shot					5-shot				
		Fold-0	Fold-1	Fold-2	Mean ↑	FB-IoU ↑	Fold-0	Fold-1	Fold-2	Mean ↑	FB-IoU ↑
ResNet-50	SCL (CVPR2021) (Zhang et al., 2021a)	49.08	35.61	48.15	44.28	61.66	50.69	35.64	48.72	45.02	62.63
	ASGNet (CVPR2021) (Li et al., 2021)	48.59	36.82	46.65	44.02	62.36	53.01	37.44	52.18	47.54	64.63
	CyCTR (NeurIPS2021) (Zhang et al., 2021b)	51.15	38.40	53.79	47.78	62.86	51.91	39.01	54.83	48.58	63.81
	PFENet (TPAMI2022) (Tian et al., 2022)	51.34	38.79	52.26	47.46	63.34	54.71	41.51	54.45	50.22	64.99
	NTRENet (CVPR2022) (Liu et al., 2022a)	49.52	38.66	51.87	46.68	62.84	50.60	40.99	55.07	48.89	63.74
	DCPNet (IJCV2023) (Lang et al., 2024)	48.43	37.59	52.09	46.04	62.76	50.34	40.75	51.33	47.47	64.10
	SCCAN (ICCV2023) (Xu et al., 2023)	52.24	38.60	52.84	47.89	63.26	52.75	38.95	54.26	48.65	62.23
	BAM (TPAMI2023) (Lang et al., 2023c)	58.17	42.12	50.95	50.41	67.03	62.51	43.16	58.24	54.64	67.92
	R2Net (TGRS2023) (Lang et al., 2023b)	56.81	39.85	49.02	48.56	62.65	60.47	41.43	50.24	50.71	65.70
	DMNet (TGRS2023) (Bi et al., 2023)	54.45	40.68	53.60	49.58	64.46	57.67	41.06	55.28	51.34	65.81
ResNet-101	SCL (CVPR2021) (Zhang et al., 2021a)	47.59	36.90	45.21	43.23	61.71	48.94	38.01	46.21	44.39	60.93
	ASGNet (CVPR2021) (Li et al., 2021)	47.55	38.47	49.28	45.10	62.03	53.54	38.24	53.20	48.33	65.35
	CyCTR (NeurIPS2021) (Zhang et al., 2021b)	50.89	38.89	52.22	47.33	62.35	52.15	40.28	55.32	49.25	64.45
	PFENet (TPAMI2022) (Tian et al., 2022)	50.69	38.37	52.85	47.30	62.46	54.40	41.55	50.55	48.83	64.57
	NTRENet (CVPR2022) (Liu et al., 2022a)	50.33	38.73	51.23	46.76	63.25	53.24	41.87	51.53	48.88	64.16
	DCPNet (IJCV2023) (Lang et al., 2024)	47.63	38.80	49.34	45.26	62.56	50.68	40.02	54.52	48.41	62.96
	SCCAN (ICCV2023) (Xu et al., 2023)	52.71	38.76	53.45	48.31	62.72	53.85	39.11	54.56	49.17	64.27
	BAM (TPAMI2023) (Lang et al., 2023c)	59.10	41.65	50.54	50.43	66.05	61.57	42.32	55.34	53.08	66.42
	R2Net (TGRS2023) (Lang et al., 2023b)	57.74	39.76	48.45	48.65	63.38	58.83	40.58	49.69	49.70	63.79
	DMNet (TGRS2023) (Bi et al., 2023)	54.01	40.04	53.57	49.21	64.03	55.70	41.69	56.47	51.29	65.88
ViT-B/16	FPTans (NeurIPS2022) (Zhang et al., 2022c)	50.04	36.85	53.30	46.73	62.36	57.92	47.42	64.23	56.52	66.12
	AgMTR (Ours)	55.45	40.67	53.81	49.98	63.20	59.05	47.86	64.08	57.00	67.60
DeiT-B/16	FPTans (NeurIPS2022) (Zhang et al., 2022c)	51.59	37.79	52.85	47.41	62.52	58.52	47.24	65.37	57.04	67.63
	AgMTR (Ours)	57.51	43.54	53.69	51.58	64.63	61.51	49.23	64.05	58.26	68.72

epochs. For PASCAL-5ⁱ, we resize the images to 480×480 and set 30 epochs, and for COCO-20ⁱ, we resize the images to 480×480 and set 40 epochs. The same data enhancements are utilized to enable fair comparisons with previous work.

For the proposed model, two transformers, i.e., ViT (Dosovitskiy et al., 2020) and DeiT (Touvron et al., 2021), are utilized as the feature encoder, and both of them are pre-trained on ImageNet (Deng et al., 2009). In the experiment, the number of agents N_a , unlabeled images N_u , pixel sets obtained through SLIC N_s , and SAB layers N are set to 5, 5, 100, and 7, respectively. The weight γ to balance two losses is set to 0.8.

5.1.3 Evaluation Metrics

Following previous FSS schemes (Lang et al., 2023c), we adopt the class mean intersection-over-union (mIoU) and foreground-background IoU (FB-IoU) as the evaluation metrics. The former calculates the averaged segmentation accuracy between different classes, while the latter calculates the accuracy between foreground and background. The mIoU evaluation metric is calculated as: $mIoU = \frac{1}{n} \sum_{i=1}^{N_{\text{unseen}}} IoU_i$, where N_{unseen} indicates the number of unseen classes in

each fold and IoU_i indicates the IoU score of the class i . And the FB-IoU metric is calculated as: $FB-IoU = (IoU_F + IoU_B) / 2$, where IoU_F and IoU_B indicate the foreground and background IoU scores, respectively.

5.2 Comparison with State-of-the-arts

5.2.1 Quantitative Results

iSAID: Table 1 quantitatively depicts the comparison between the proposed and other methods on iSAID benchmark. Satisfyingly, our AgMTR achieves state-of-the-art performance in all cases. For example, under the 1-shot setting, AgMTR with DeiT-B/16 backbone achieves 51.58% mIoU, outperforming the best CNN-based method BAM (Lang et al., 2023c) by 1.15% and the Transformer-based method FPTans (Zhang et al., 2022c) by 4.17%. Surprisingly, AgMTR under the 1-shot setting even beats several methods under the 5-shot setting, e.g., R2Net (Lang et al., 2023b), DMNet (Bi et al., 2023), and SCCAN (Xu et al., 2023), which fully demonstrates that our method can alleviate the pressure of dense annotation and easily generalize to unseen classes. Un-

Table 2 Performance comparison on PASCAL-5ⁱ benchmark measured in mIoU (%) under the 1- and 5-shot settings. The ‘Mean’ indicates the averaged mIoU accuracy for all classes under all folds.

Backbone	Method	1-shot					5-shot				
		Fold-0	Fold-1	Fold-2	Fold-3	Mean \uparrow	Fold-0	Fold-1	Fold-2	Fold-3	Mean \uparrow
ResNet-50	CyCTR (NeurIPS2021) (Zhang et al., 2021b)	65.70	71.00	59.50	59.70	63.98	69.30	73.50	63.80	63.50	67.53
	PFENet (TPAMI2022) (Tian et al., 2022)	61.70	69.50	55.40	56.30	60.73	63.10	70.70	55.80	57.90	61.88
	HPA (TPAMI2022) (Cheng et al., 2022b)	65.94	71.96	64.66	56.78	64.84	70.54	73.28	68.37	63.41	68.90
	AAFormer (ECCV2022) (Wang et al., 2022d)	69.10	73.30	59.10	59.20	65.18	72.50	74.70	62.00	61.30	67.63
	NTRENet (CVPR2022) (Liu et al., 2022a)	65.40	72.30	59.40	59.80	64.23	66.20	72.80	61.70	62.20	65.73
	IPMT (NeurIPS2022) (Liu et al., 2022b)	72.80	73.70	59.20	61.60	66.83	73.10	74.70	61.60	63.40	68.20
	BAM (TPAMI2023) (Lang et al., 2023c)	69.15	74.66	67.79	61.72	68.33	71.84	75.67	71.95	67.54	71.75
	DCPNet (IJCV2023) (Lang et al., 2024)	67.20	72.90	65.20	59.40	66.10	70.50	75.30	68.00	67.70	70.30
	SCCAN (ICCV2023) (Xu et al., 2023)	68.30	72.50	66.80	59.80	66.80	72.30	74.10	69.10	65.60	70.30
	HDMNet (CVPR2023) (Peng et al., 2023)	71.00	75.40	68.90	62.10	69.35	71.30	76.20	71.30	68.50	71.83
	MIANet (CVPR2023) (Yang et al., 2023)	68.51	75.76	67.46	63.15	68.72	70.20	77.38	70.02	68.77	71.59
	RiFeNet (AAAI2024) (Bao et al., 2023)	68.40	73.50	67.10	59.40	67.10	70.00	74.70	69.40	64.20	69.60
ResNet-101	CyCTR (NeurIPS2021) (Zhang et al., 2021b)	67.20	71.10	57.60	59.00	63.73	71.00	75.00	58.50	65.00	67.38
	PFENet (TPAMI2022) (Tian et al., 2022)	60.50	69.40	54.40	55.90	60.05	62.80	70.40	54.90	57.60	61.43
	AAFormer (ECCV2022) (Wang et al., 2022d)	69.90	73.60	57.90	59.70	65.28	75.00	75.10	59.00	63.20	68.08
	NTRENet (CVPR2022) (Liu et al., 2022a)	65.50	71.80	59.10	58.30	63.68	67.90	73.20	60.10	66.80	67.00
	IPMT (NeurIPS2022) (Liu et al., 2022b)	71.60	73.50	58.00	61.20	66.08	75.30	76.90	59.60	65.10	69.23
	HPA (TPAMI2022) (Cheng et al., 2022b)	66.40	72.65	64.10	59.42	65.64	68.02	74.60	65.85	67.11	68.90
	BAM (TPAMI2023) (Lang et al., 2023c)	69.88	75.37	67.06	62.11	68.61	72.62	77.06	70.67	69.82	72.54
ViT-B/16	DCPNet (IJCV2023) (Lang et al., 2024)	68.90	74.20	63.30	62.70	67.30	72.10	77.10	66.50	70.50	71.50
	SCCAN (ICCV2023) (Xu et al., 2023)	70.90	73.90	66.80	61.70	68.30	73.10	76.40	70.30	66.10	71.50
FPTrans (NeurIPS2022) (Zhang et al., 2022c)	FPTrans (NeurIPS2022) (Zhang et al., 2022c)	67.10	69.80	65.60	56.40	64.73	73.50	75.70	77.40	68.30	73.73
	AgMTR (Ours)	70.17	74.68	67.15	58.20	67.55	73.55	76.84	74.75	66.78	72.98
DeiT-B/16	FPTrans (NeurIPS2022) (Zhang et al., 2022c)	72.30	70.60	68.30	64.10	68.83	76.70	79.00	81.00	75.10	77.95
	MuHS (ICLR2023) (Hu et al., 2022)	71.20	71.50	67.00	66.60	69.08	75.70	77.80	78.60	74.70	76.70
	AgMTR (Ours)	72.13	75.72	66.31	66.91	70.27	76.44	78.54	75.56	74.95	76.37

der the 5-shot setting, AgMTR achieves 3.62% gains over the best BAM. Similar gains are realized in FB-IoU. The above results strongly prove that our agent-level semantic correlation can effectively handle large intra-class variations and complex backgrounds in remote sensing scenarios, realizing excellent segmentation performance for unseen classes.

PASCAL-5ⁱ and COCO-20ⁱ: We also explore the performance of the proposed method in more common natural scenarios to further explore its generalization and applicability. Table 2-3 present the 1- and 5-shot results on PASCAL-5ⁱ and COCO-20ⁱ. Encouragingly, our AgMTR performs equally competitively. Specifically, for PASCAL-5ⁱ, AgMTR with DeiT-16/B backbone outperforms the top CNN method HDMNet (Peng et al., 2023) by 0.92% and 4.54% under the 1- and 5-shot settings, respectively. Besides, in comparison with the transformer-based methods FPTrans (Zhang et al., 2022c) and MuHS (Hu et al., 2022), we realize a lead of 1.44% and 1.19% mIoU under the 1-shot setting. And for COCO-20ⁱ with larger object differences and more complex backgrounds, similar gains can be realized as well. For

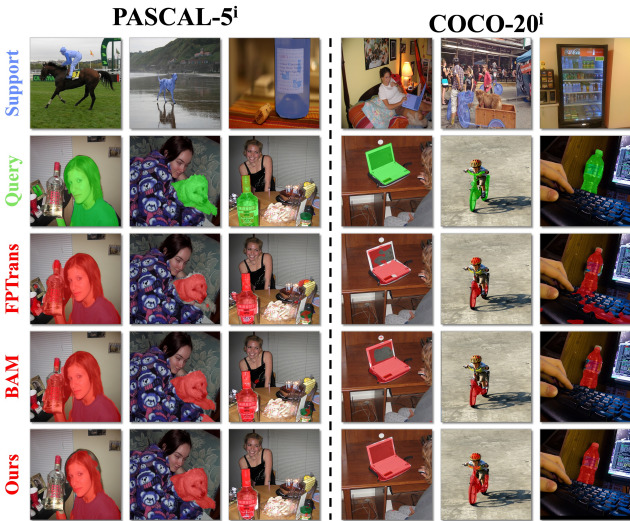
instance, AgMTR exceeds the top CNN-based method MIANet (Yang et al., 2023) and the Transformer-based method MuHS (Hu et al., 2022) by 0.81% and 1.66%, respectively, under the 1-shot setting. The above results indicate that our method is general enough to be applied to various domains.

5.2.2 Qualitative Results

To further exhibit the excellence of the proposed AgMTR, we visualize several segmentation results on three FSS datasets. Fig. 7 illustrates the qualitative results on iSAID. One can find that our method has clear advantages: (i) Benefiting from mining class-specific semantics from support images, unlabeled images, and the query image, our agents have more powerful class-awareness to perform precise agent-level semantic correlation, thus effectively focusing on the interested class while suppressing the activation of other classes. For instance, for the dense small targets ‘small vehicles’ in 4th column and the ‘harbor’ with irrelevant classes interference in 7th column, R2Net incorrectly activates the ‘Roof’ and

Table 3 Performance comparison on COCO-20ⁱ benchmark measured in mIoU (%) under the 1- and 5-shot settings. The ‘Mean’ indicates the averaged mIoU accuracy for all classes under all folds.

Backbone	Method	1-shot					5-shot				
		Fold-0	Fold-1	Fold-2	Fold-3	Mean \uparrow	Fold-0	Fold-1	Fold-2	Fold-3	Mean \uparrow
ResNet-50	CyCTR (NeurIPS2021) (Zhang et al., 2021b)	38.90	43.00	39.60	39.80	40.33	41.10	48.90	45.20	47.00	45.55
	PFENet (TPAMI2022) (Tian et al., 2022)	36.50	38.60	34.50	33.80	35.85	36.50	43.30	37.80	38.40	39.00
	HPA (TPAMI2022) (Cheng et al., 2022b)	40.30	46.57	44.12	42.71	43.43	45.54	55.43	48.90	50.21	50.02
	AAFormer (ECCV2022) (Wang et al., 2022d)	39.80	44.60	40.60	41.40	41.60	42.90	50.10	45.50	49.20	46.93
	NTRENet (CVPR2022) (Liu et al., 2022a)	36.80	42.60	39.90	37.90	39.30	38.20	44.10	40.40	38.40	40.28
	IPMT (NeurIPS2022) (Liu et al., 2022b)	41.40	45.10	45.60	40.00	43.03	43.50	49.70	48.70	47.90	47.45
	BAM (TPAMI2023) (Lang et al., 2023c)	43.86	51.38	47.86	44.47	46.89	49.76	55.43	52.31	50.19	51.92
	DCPNet (IJCV2023) (Lang et al., 2024)	43.00	48.60	45.40	44.80	45.50	47.00	54.70	51.70	50.00	50.90
	SCCAN (ICCV2023) (Xu et al., 2023)	40.40	49.70	49.60	45.60	46.30	47.20	57.20	59.20	52.10	53.90
	MIANet (CVPR2023) (Yang et al., 2023)	42.49	52.95	47.77	47.42	47.66	45.84	58.18	51.29	51.90	51.80
RiFeNet (AAAI2024) (Bao et al., 2023)	39.10	47.20	44.60	45.40	44.10	44.30	52.40	49.30	48.40	48.60	
ResNet-101	PFENet (TPAMI2022) (Tian et al., 2022)	34.40	33.00	32.30	30.10	32.45	38.50	38.60	38.20	34.30	37.40
	NTRENet (CVPR2022) (Liu et al., 2022a)	38.30	40.40	39.50	38.10	39.08	42.30	44.40	44.20	41.70	43.15
	IPMT (NeurIPS2022) (Liu et al., 2022b)	40.50	45.70	44.80	39.30	42.58	45.10	50.30	49.30	46.80	47.88
	HPA (TPAMI2022) (Cheng et al., 2022b)	43.08	50.01	44.78	45.19	45.77	49.18	57.76	51.97	50.64	52.39
	SCCAN (ICCV2023) (Xu et al., 2023)	42.60	51.40	50.00	48.80	48.20	49.40	61.70	61.90	55.00	57.00
DeiT-B/16	FPTans (NeurIPS2022) (Zhang et al., 2022c)	44.40	48.90	50.60	44.00	46.98	54.20	62.50	61.30	57.60	58.90
	MuHS (ICLR2023) (Hu et al., 2022)	44.00	50.00	49.10	46.30	47.35	53.60	60.50	57.30	55.20	56.65
	AgMTR (Ours)	44.01	55.51	49.90	46.61	49.01	52.51	62.10	59.64	53.61	56.97

**Fig. 8** Qualitative visualization of our AgMTR and several competing methods under the 1-shot setting on more common natural scenarios. The left panel shows the PASCAL-5ⁱ results while the right shows the COCO-20ⁱ results. From top to bottom, each row represents: support images with GT (blue), query images with GT (green), segmentation results of FPTans (red), segmentation results of BAM (red), and our segmentation results (red).

‘Boats’, respectively, while our AgMTR segments nicely. (ii) Benefiting from the local semantic exploration of the target category, our AgMTR can reasonably find the local agent that best matches the query pixel, and thus better classify the

pixel, yielding more accurate segmentation results, e.g., the ‘Storage tanks’ (2nd column) and the ‘Planes’ (5th column). When extended to common natural scenarios, the proposed AgMTR copes equally well, efficiently distinguishing between FG and BG pixels of the query image, as depicted in Fig. 8. The above advantages sufficiently prove that the proposed AgMTR can efficiently handle the FSS tasks in various scenarios and demonstrate robust generalizability.

5.3 Ablation Study and Analysis

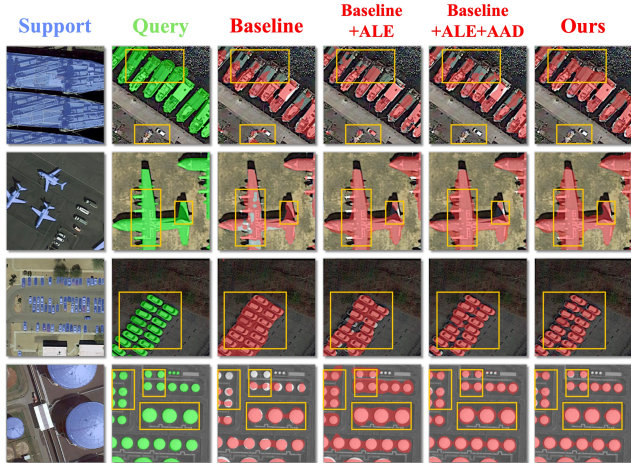
A set of ablation studies are executed to discuss and understand our proposed method thoroughly. Unless otherwise noted, the experiments in this section are conducted on iSAID utilizing the DeiT-B/16 backbone under the 1-shot setting.

5.3.1 Component Analysis

Component Analysis in Segmentation Performance: Table 4 discusses the performance impact of the component variants in AgMTR. In general, we could observe the following phenomena: (i) With the integration of Agent Learning Encoder (ALE), Agent Aggregation Decoder (AAD), and Semantic Alignment Decoder (SAD) three components, AgMTR achieves a 4.76% mIoU improvement compared to the baseline, strongly validating their effectiveness. (ii) The proposed ALE contributes the most to the final model. This

Table 4 Ablation study of the segmentation performance for the component variants in AgMTR under the 1-shot setting on iSAID. Δ denotes the performance (mIoU) gain compared to the baseline.

#	Support (ALE)	Unlabeled (AAD)	Query (SAD)	mIoU \uparrow	FB-IoU \uparrow	Δ
(a)	\times	\times	\times	46.82	61.12	-
(b)	\checkmark	\times	\times	48.94	62.68	2.12
(c)	\checkmark	\checkmark	\times	50.01	<u>63.04</u>	3.19
(d)	\checkmark	\times	\checkmark	<u>50.27</u>	62.96	3.45
(e)	\checkmark	\checkmark	\checkmark	51.58	64.63	4.76

**Fig. 9** Qualitative visualization of AgMTR variants and the Baseline. From left to right, each column represents: Support images (GT), Query images (GT), results with the Baseline, results with the Baseline+ALE, results with the Baseline+ALE+AAD, results with the Baseline+ALE+AAD+SAD (i.e., AgMTR). Several typical areas are marked with yellow boxes.

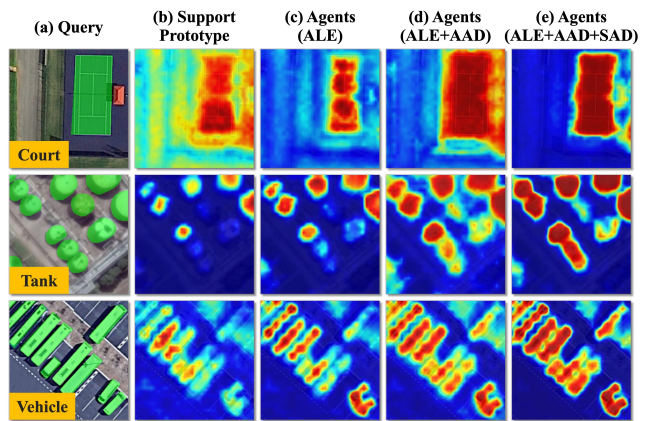
is possible because mining class-specific semantics from the support images is the most essential and fundamental step. Only when sufficiently valid semantics are mined can agents stably mine interested semantics from unlabeled and query images without introducing irrelevant noise. This also validates the effectiveness of the proposed agent paradigm to some extent. (iii) in case (c) and case (d), the introduction of AAD and SAD yields 1.07% and 1.33% gains, respectively, which quantitatively validates that the aggregation of class-specific semantics from unlabeled and query images for agents can facilitate breaking through the limited support set and better guide query segmentation. (IV) Besides, we present the segmentation results for different variants as shown in Fig. 9. By introducing components step by step, the segmentation results are further improved, qualitatively verifying the effectiveness and necessity of the proposed components.

Component Analysis in Complexity: To investigate the time complexity of the different components in AgMTR, we conduct an ablation study on the iSAID dataset, with the

Table 5 Ablation study of the time complexity for the component variants in AgMTR. ‘GFLOPs’ denote the floating point operations of the model and ‘Inference Speed (FPS)’ denotes the number of images the model can infer per second.

Method	mIoU	GFLOPs	Inference Speed (FPS)
IPMT (NeurIPS2021) (Liu et al., 2022b)	48.85	123.51	14.01
SCCAN (ICCV2023) (Xu et al., 2023)	48.31	143.37	16.45
BAM (TPAMI2023) (Lang et al., 2023c)	50.43	117.03	30.95
Baseline	46.82	47.61	79.71
Baseline+ALE	48.94	<u>48.85</u>	<u>71.26</u>
Baseline+ALE+AAD	50.01	111.18	36.89
Baseline+ALE+SAD	50.27	57.59	41.63
Baseline+ALE+AAD [†] +SAD	<u>50.64</u>	70.37	30.30
Baseline+ALE+AAD+SAD	51.58	119.93	28.74

“ALE” denotes the Agent Learning Encoder, “AAD” denotes the Agent Aggregation Decoder, and “SAD” denotes the Semantic Alignment Decoder. Notably, “AAD” employs 5 unlabeled images by default, while “AAD[†]” employs 1 unlabeled image.

**Fig. 10** Qualitative visualization of activation maps of component variants in AgMTR on the query image. As can be noticed, each component promotes the agent better to activate the specific objects in the query image.

results depicted in Table 5. The following phenomena can be derived: (i) Among the three components, AAD has the largest computational complexity. This is because AAD aims to mine class-specific information from additional unlabeled images (5 images are utilized by default), which equates to processing 7 (1 query, 1 support, and 5 unlabeled) images simultaneously, incurring additional computational costs. (ii) Despite the obvious computational cost of AAD, AgMTR achieves the best mIoU performance with the second-lowest GFLOPs compared to others, far better than SCCAN, i.e., 51.58% vs 48.31% mIoU and 119.93 vs 143.37 GFLOPs. (iii) AgMTR achieves a balance between accuracy and complexity when AAD utilizes less unlabeled images. We attempt to mine class-specific semantics with only one unlabeled image, at which point the model achieves 50.64% mIoU at 70.37 GFLOPs, balancing segmentation accuracy and computational complexity.

Table 6 Ablation study of the intra-class variance for the component variants in AgMTR by measuring the cosine distance D_{aq} between the agents and the query prototype on iSAID dataset, where the distance D_{sq} between the support prototype and the query prototype is employed as a comparison.

#	Agent Semantic Source			Cosine distance \uparrow			
	Support (ALE)	Unlabeled (AAD)	Query (SAD)	Fold-0	Fold-1	Fold-2	Mean
D_{sq}	\times	\times	\times	0.5097	0.5357	0.7076	0.5843
D_{aq}	\checkmark	\times	\times	0.6778	0.6437	0.7310	0.6842
	\checkmark	\checkmark	\times	0.7076	0.6498	0.7614	0.7063
	\checkmark	\checkmark	\checkmark	0.7678	0.7047	0.7669	0.7465

Component Analysis in Intra-class Variance: To objectively evaluate the effectiveness of the proposed three components, we employ cosine distance to measure the distance D_{aq} between the query prototype and the agents in every episode, where the distance between the query prototype and the support prototype D_{sq} serves as a comparison. The average distance of the classes in each fold and the average of all classes are listed in Table 6. Notably, multiple agents are averaged into one for computation with the query prototype. Obviously, after gradually aggregating the semantics from the support images, the unlabeled images, and the query image by driving the agents through ALE, AAD, and SAD, D_{aq} gradually increases, and is larger than D_{sq} in all folds. This phenomenon reveals that with the proposed three components, the proposed agents work significantly to reduce the distance with the query image and minimize the negative impact of large intra-class variations in remote sensing, providing better guidance for query image segmentation. We also visualize the activation maps of the agent derived from different components, as illustrated in Fig. 10. Compared to the support prototype, agents derived from different components can focus more on specific objects in the query image, enabling more precise activations. The above results fully validate the effectiveness of the three proposed components from the perspective of intra-class variance.

5.3.2 Ablation study of the Agent Learning Encoder

As mentioned in Sec. 4.2, Agent Learning Encoder (ALE) aims to mine class-specific semantics in the support images to derive local-aware agents for performing agent-level semantic correlation. The gain of 2.12% mIoU in Table 4 has quantitatively verified that the local agents generated by utilizing ALE are successful in effectively distinguishing between foreground and background pixels, generating more complete objects and more accurate boundaries (see Fig. 9). This section discusses specific details in the ALE, including the number of agents generated and the learning scheme.

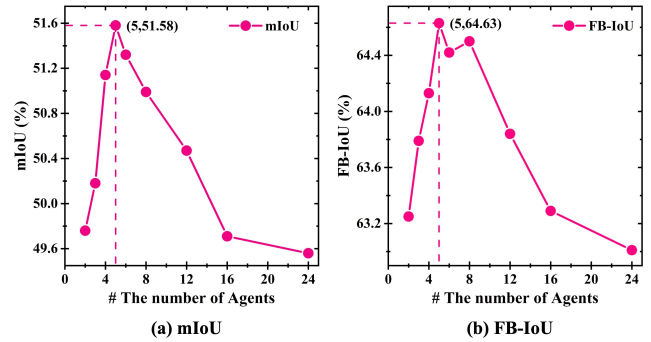


Fig. 11 Ablation study of the number of agents (i.e., N_a) on segmentation performance. The best segmentation accuracy is obtained with the number of agents set to 5, i.e., $N_a = 5$.

Table 7 Ablation study of different initialization and learning schemes of agents in ALE.

#	Initialization	OT	Fold-0	Fold-1	Fold-2	Mean	FB-IoU
(a)	Random	\checkmark	52.50	41.87	53.00	49.12	63.44
(b)	Random+Sup	\times	55.64	42.36	54.22	50.74	63.82
(c)	Random+Sup	\checkmark	57.51	43.54	53.69	51.58	64.63

Firstly, we investigate the impact of the number of agents (i.e., N_a) on segmentation performance, as depicted in Fig. 11. It can be found that as the number of agents (i.e., N_a) increases from 1 to 5, the segmentation accuracy will gradually increase, especially with 51.58% mIoU achieved for $N_a = 5$. It is reasonable because the support mask will be divided into more delicate local regions, thus driving the agent to aggregate finer-grained local semantics. However, when continuing to increase N_a , the segmentation accuracy begins to decrease. At this point, the support mask becomes forced to be divided into more unreasonable local masks, such as dividing the left and right ‘Wings’ of the ‘Plane’, which leads to different agents aggregating similar semantics, resulting in redundancy and even interference.

We then explore the performance impact of different initialization and learning schemes of agents in ALE, as illustrated in Table 7. In these schemes, ‘Random’ and ‘Random+Sup’ denote randomly initialized tokens, and the addition of the support prototype with randomly initialized tokens as initial agents, respectively. ‘OT’ denotes dividing the support mask into local masks with the optimal transport algorithm. From the table, we can observe the following phenomena: (i) Utilizing only randomly initialized tokens as the initial agents is suboptimal (case (a)) since the agents lack class-specific semantics to guide the capture of similar object semantics. Instead, dependent on class-specific semantics in the support prototype (case (c)), the agents can continue to assimilate similar semantics in subsequent processes, thus further enhancing class-awareness. (ii) After introducing the optimal transport (OT) to adaptively generate local masks,

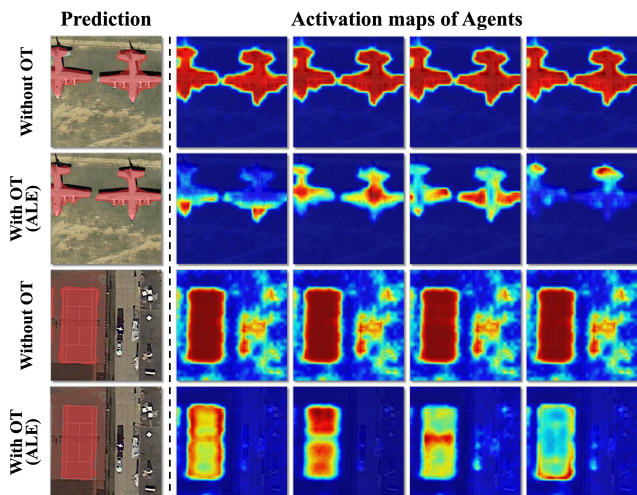


Fig. 12 Qualitative visualization of activation maps of different agents on the query image, where ‘with/without OT’ denotes whether ALE employs OT to generate multiple local masks.

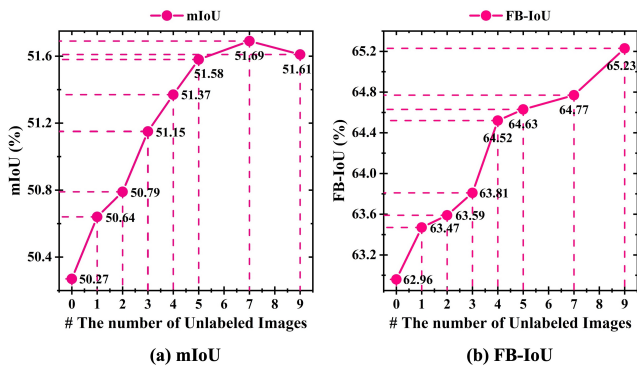


Fig. 13 Ablation study of the number of unlabeled images (i.e., N_u) on segmentation performance in AAD. As the number increases, the segmentation accuracy gradually improves, especially for FB-IoU.

ALE can drive different agents to aggregate the interested semantics under different local masks. The comparison between case (b) and case (c) proves the effectiveness of the above scheme. Fig.12 also visualizes the activation maps of different agents on the query image after generating local masks employing optimal transport (OT). It can be found that equipped with OT, ALE can drive different agents to focus on different local regions of the specific object. When OT is not employed, not only the generated agents do not have local-awareness and produce coarser activations, but also different agents will aggregate similar semantics and produce redundancy. The above phenomenon effectively proves the effectiveness and necessity of employing OT to explore local semantics in ALE.

5.3.3 Ablation study of the Agent Aggregation Decoder

As mentioned in Sec.4.3, Agent Aggregation Decoder (AAD) aims to mine semantic information in unlabeled images that

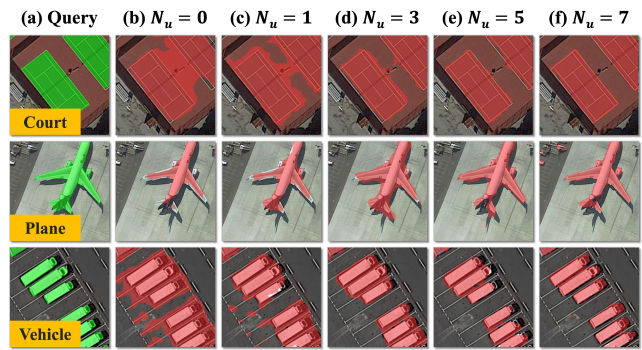


Fig. 14 Qualitative visualization with different numbers of unlabeled images in AAD.

Table 8 Ablation study of the number of unlabeled images (i.e., N_u) on computational complexity measured in GFLOPs.

N_u	0	1	2	3	4	5	7	9
mIoU	50.27	50.64	50.79	51.15	51.37	51.58	51.69	51.61
GFLOPs	57.59	70.37	82.92	95.46	107.57	119.93	143.77	166.83

Table 9 Ablation study of the Graph Attention Network (GAT) in AAD.

#	GAT	Fold-0	Fold-1	Fold-2	Mean	FB-IoU
(a)	✗	56.22	41.61	54.83	50.89	63.76
(b)	✓	57.51	43.54	53.69	51.58	64.63

are beneficial to the current task, for breaking the limitations of the support set and enabling stronger generalization. The quantitative results in Table 6 demonstrate that AAD can effectively mine class-specific semantics in unlabeled data sources, flexibly dealing with intra-class variance. A natural discussion is about how many unlabeled images (i.e., N_u) are the most appropriate. Fig.13 explores the impact of the number of unlabeled images (i.e., N_u) on segmentation performance. As the number of unlabeled images increases, AAD can mine richer class-specific semantics from the larger number of unlabeled images, thus further optimizing the agents to break through the limited support set and better guide query segmentation. The above observation is also qualitatively demonstrated by the segmentation results with different numbers of unlabeled images in Fig.14. Considering the efficiency of the model (see Table 8), N_u is set to 5 in the experiments. We then investigate the impact of Graph Attention Network (GAT) on performance in AAD, as illustrated in Table 9. It can be found that 0.69% mIoU and 0.87% FB-IoU improvement is realized after introducing GAT, which is a good demonstration that GAT can enhance the contextual semantics of unlabeled prototypes and thus be efficiently captured by local agents.

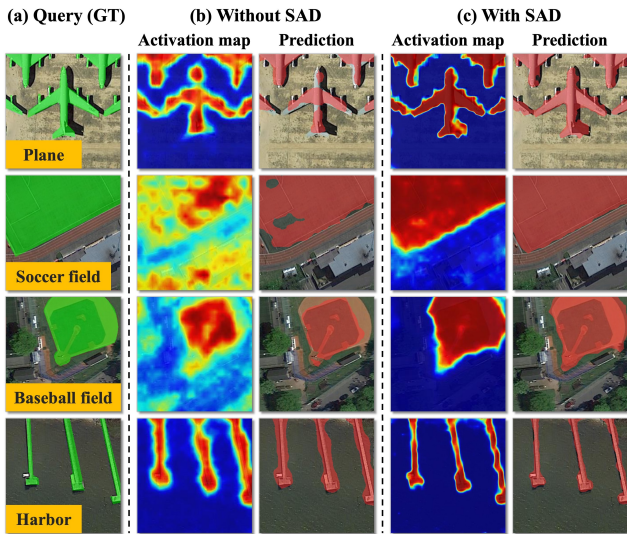


Fig. 15 Qualitative visualization of Semantic Alignment Decoder (SAD). (a) Query image with GT. (b) Activation map and prediction result without SAD. (c) Activation map and prediction result with SAD.

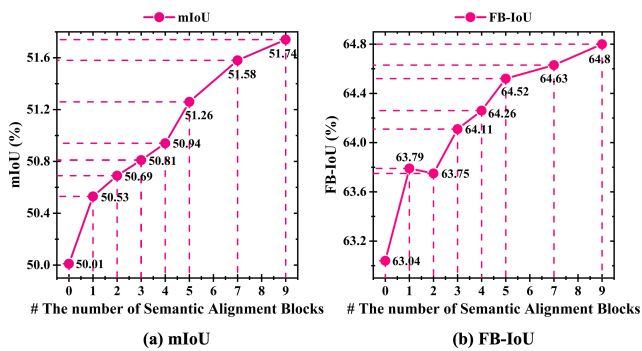


Fig. 16 Ablation study of the number of Semantic Alignment Blocks (i.e., N) on segmentation performance in SAD.

Table 10 Ablation study of the contribution γ of Agent Segmentation Loss \mathcal{L}_{ASL} to total loss in Eq.(15).

\mathcal{L}_{ASL}	0.0	0.2	0.4	0.6	0.8	1.0
mIoU	51.30	51.19	51.27	51.45	51.58	51.51
FB-IoU	64.46	64.45	64.07	64.26	64.63	64.39

5.3.4 Ablation study of the Semantic Alignment Decoder

As mentioned in Sec.4.4, Semantic Alignment Decoder (SAD) aims to mine the class-specific semantics of the query image itself to promote semantic alignment with the query object, and this paradigm of mining one’s own semantics to guide one’s own segmentation can cope well with large intra-class variations. We explore the distance with the query object in feature space, with the results shown in Table 6, which quantitatively demonstrates the effectiveness of SAD in bringing the distance with the query object closer. The visualization results in Fig.15 also qualitatively validate that the proposed SAD can further mine the query image class-

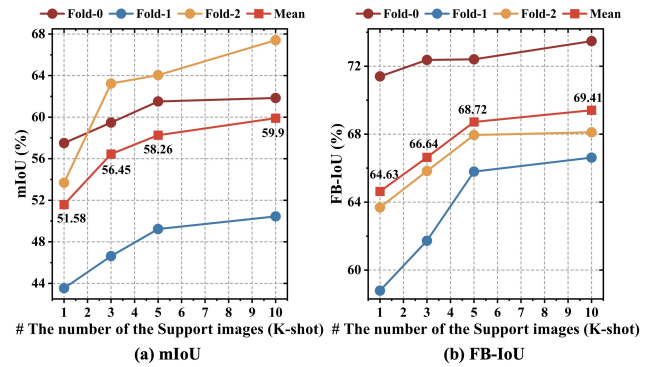


Fig. 17 Ablation study of the number of support images (i.e., K -shot) on segmentation performance.

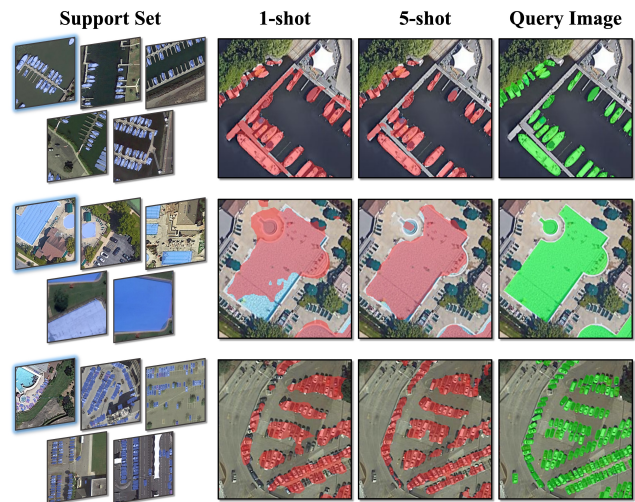


Fig. 18 Comparison results of our method under the 1- and 5-shot settings on iSAID dataset. The first labeled image (blue border) in the Support Set is sampled for 1-shot segmentation.

specific semantics to achieve more precise boundaries and fewer false activations.

Further, we explore the impact of the number of Semantic Alignment Blocks (i.e., N) on segmentation performance, as depicted in Fig.16. As the number N increases, SAD can further improve the quality of the pseudo-local masks of the query image, which enables the agents to better aggregate the local semantics from the query image, achieving better segmentation, especially receiving 51.74% mIoU and 64.80% FB-IoU when $N = 9$. Considering the efficiency of the model, $N = 7$ is a proper choice. In addition, Table 10 gives the impact of the contribution γ of the Agent Segmentation Loss \mathcal{L}_{ASL} in SAD. It can be observed that the segmentation accuracy shows an increasing and then decreasing trend, and reaches the best performance when $\gamma = 0.8$.

5.3.5 Ablation study of K -shot

When expanded to the K -shot ($K > 1$) setting, the support set can provide more labeled samples for guiding segmen-

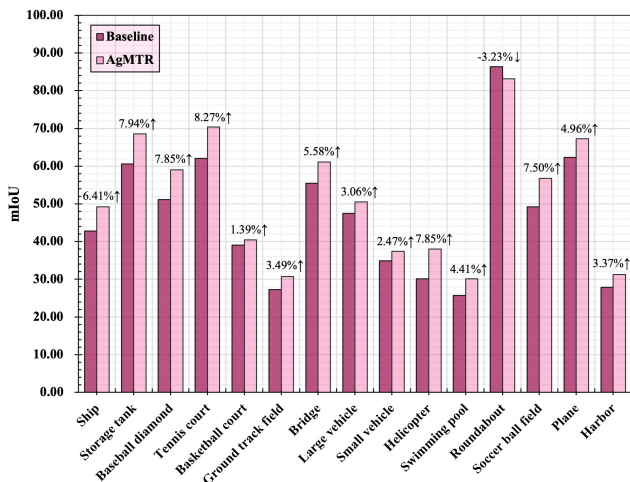


Fig. 19 Performance comparison (mIoU) of our AgMTR and the Baseline in different classes on iSAID under the 1-shot setting.

tation. Fig. 17 demonstrates the impact on performance in iSAID with different numbers of support images provided. It can be noticed that the mIoU of each Fold achieves a large improvement as K keeps increasing. When continuing to increase to 10 images, the boost slows down, which is reasonable because of the decreasing marginal effect of the labeled samples. Fig. 18 also compares the segmentation results of the proposed AgMTR under the 1- and 5-shot settings. The 5-shot results are significantly superior to the 1-shot results with more complete objects and fewer false activations. The insight behind this phenomenon is that AgMTR can mine more class-representative and stable agents from more support images, which can further facilitate agents to capture similar semantics from unlabeled and query images for more precise agent-level semantic correlations.

5.3.6 Performance Analysis for Each Class

Fig. 19 compares the segmentation performance of our AgMTR with the baseline in different classes on iSAID. Our method achieves significant advantages in 14 out of 15 classes, especially for the ‘Storage tank’, ‘Baseball field’, ‘Tennis court’, ‘Helicopter’, and ‘Soccer field’ classes achieving more than 7% gains. We observe that these classes tend to have large intra-class differences, requiring the FSS model to be more class-aware. However, our method performs worse than the baseline for the ‘Roundabout’ class, i.e., 83.14% vs 85.27%. It may be due to the fact that the appearance of this class tends to be regular and no other classes are interfering in the image, the baseline method can easily tackle it as well.

5.3.7 Ablation study of the Backbone

Table 11 gives the impact of different backbones on segmentation performance, where the inference speed is measured under the 5-shot setting. We can observe the following

Table 11 Ablation study of the Backbone in the proposed AgMTR, where the inference speed is measured under the 5-shot setting.

#	Backbone	1-shot		5-shot		Inference Speed (FPS)
		mIoU	FB-IoU	mIoU	FB-IoU	
(a)	ViT-S/16	48.70	61.79	55.45	66.57	25.02
(b)	ViT-B/16	<u>49.98</u>	<u>63.20</u>	<u>57.00</u>	<u>67.62</u>	18.45
(c)	DeiT-T/16	46.84	61.28	54.70	65.99	<u>23.91</u>
(d)	DeiT-S/16	49.11	62.52	55.33	66.31	22.49
(e)	DeiT-B/16	51.58	64.63	58.26	68.72	19.68

phenomena: (i) Employing the backbone of DeiT-B/16 realizes the optimal accuracy in all settings, followed by the backbone of ViT-B/16. (ii) Employing the backbone of DeiT-S/16 (89MB) yields a segmentation accuracy on par with the ResNet-101 (179MB) based method DMNet, i.e., 49.11% vs 49.21%, which clearly demonstrates the superiority of the proposed method. (iii) ViT-S/16 and DeiT-T/16 have slightly worse segmentation performance, but they have faster inference speeds than others.

5.3.8 Visualization of Local-aware Agents

To further explore and understand the role of the local-aware agents, Fig. 20 exhibits the visualization of activation maps of different agents on the query image, which are derived by performing similarity computation between the agents and the query features. We could observe the following phenomena: (i) Different agents are able to focus on different yet complementary local regions, which strongly demonstrates the effectiveness of the local semantic mining as conceived. (ii) The constructed agents can reasonably focus on key semantic clues in the current episode, e.g., in the first column, different agents will focus on the ‘Fuselage’, ‘Wings’, and ‘Tail’ of the multiple ‘Planes’. And this rationalization is more obvious in simpler natural scenarios (PASCAL-5ⁱ). This also proves the generalizability of the proposed method from another perspective.

5.4 Extension in Weak-label Few-shot Segmentation

To further alleviate the burden of dense labeling in the real world, this section discusses the effectiveness of FSS with two cheaper mask schemes, bounding box and scribble. Following the setup of (Wang et al., 2019), the above cheaper schemes are randomly generated from the original dense labeled masks of support images, as shown in Fig. 21. Table 12 demonstrates the performance of different mask schemes on three benchmarks under the 1-shot setting. One can find that our method with the scribble mask can achieve 48.88%, 67.09%, and 44.43% mIoU accuracy on three benchmarks,

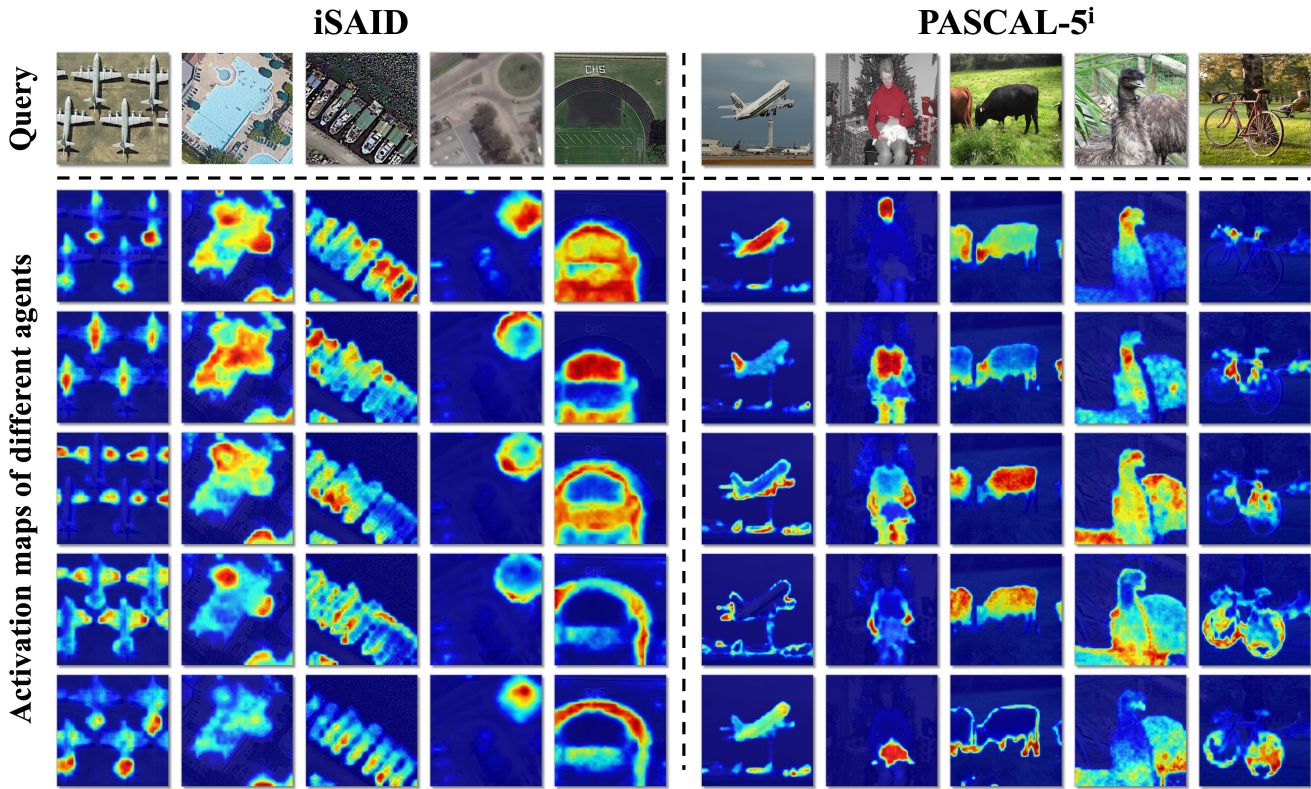


Fig. 20 Qualitative visualization of activation maps of the proposed agents on the query image in iSAID and PASCAL-5ⁱ. Obviously, different agents reasonably focus on different local regions. This is because the proposed three components could explore valuable local semantics from the support, unlabeled, and query images to empower the agents with local-awareness.

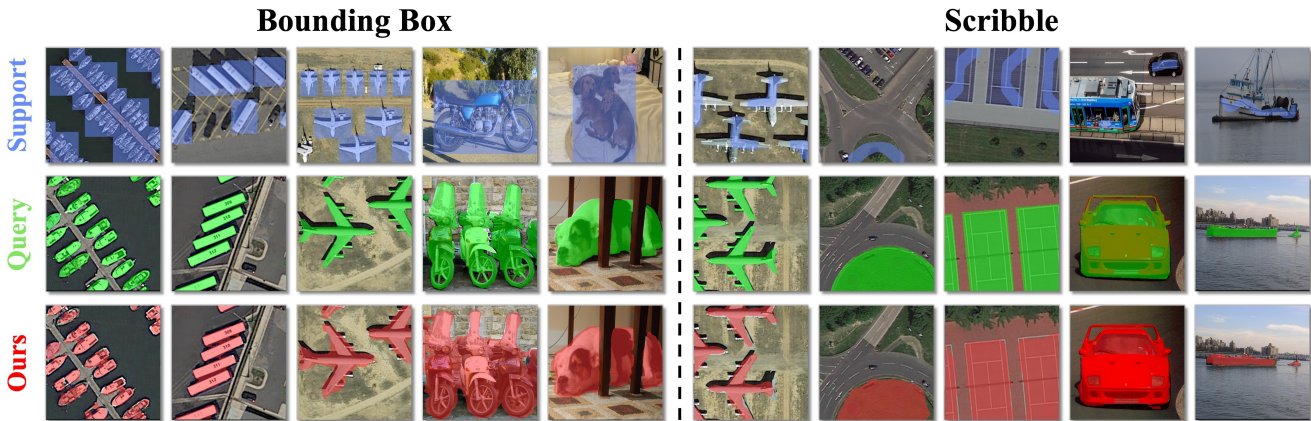


Fig. 21 Qualitative visualization results for Weak-label Few-shot Segmentation under the 1-shot setting. The left panel shows the results of employing bounding box masks, while the right panel shows the results of employing scribble masks. From top to bottom, each row represents: support images with GT (blue), query images with GT (green), our segmentation results (red).

respectively, which performs comparably with several competing methods with the dense mask, revealing AgMTR’s tolerance to label quality. In addition, we notice that employing the bounding box mask provides weaker results than the scribble mask, which may be due to the fact that the bounding box mask contains a large amount of background noise that interferes with the mining of valuable semantics from the support images by AgMTR. Based on the above observations,

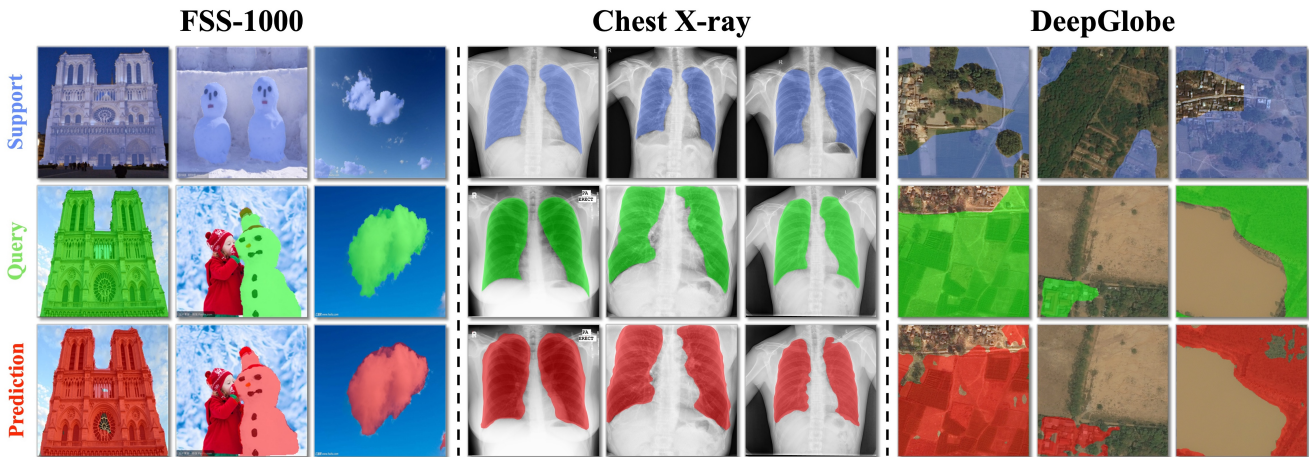
we believe that the scribble mask can effectively alleviate the labeling burden while maintaining excellent performance.

5.5 Extension in Cross-domain Few-shot Segmentation

To explore the generalization of the proposed AgMTR to unseen domains in real-world situations, we perform the Cross-domain Few-shot Segmentation, where the samples

Table 12 Extended experiments of Weak-label Few-shot Segmentation on three FSS benchmarks measured in mIoU (%) under the 1-shot setting. ‘Dense’ denotes the densely labeled mask. ‘Bounding box’ and ‘Scribble’ denote the bounding box label and scribble label, respectively.

Method	Scheme	iSAID				PASCAL-5 ⁱ					COCO-20 ⁱ				
		Fold-0	Fold-1	Fold-2	Mean	Fold-0	Fold-1	Fold-2	Fold-3	Mean	Fold-0	Fold-1	Fold-2	Fold-3	Mean
DCPNet (IJCV2023)	Dense	48.43	37.59	52.09	46.04	67.20	72.90	65.20	59.40	66.10	43.00	48.60	45.40	44.80	45.50
FPTrans (NeurIPS2022)	Dense	51.59	37.79	52.85	47.41	72.30	70.60	68.30	64.10	68.83	44.40	48.90	50.60	44.00	46.98
AgMTR (Ours)	Bbox	55.19	38.98	48.70	47.62	59.03	64.51	55.44	56.49	58.81	32.65	43.40	38.14	43.50	39.42
	Scribble	56.20	40.75	49.68	48.88	67.92	73.45	62.30	64.69	67.09	37.22	49.84	45.73	44.97	44.43
	Dense	57.51	43.54	53.69	51.58	72.13	75.72	66.31	66.91	70.27	44.01	55.51	49.90	46.61	49.01

**Fig. 22** Qualitative visualization results for Cross-domain Few-shot Segmentation under the 1-shot setting, where the model is trained on PASCAL VOC dataset and evaluated on three datasets, including FSS-1000, Chest X-ray, and DeepGlobe.**Table 13** Extended experiments of Cross-domain FSS on three datasets. Notably, the proposed model is trained on PASCAL VOC and evaluated on these three datasets. Some comparison results are from (Herzog, 2024) and (Lei et al., 2022).

Method	1-shot				5-shot			
	FSS-1000	X-ray	Deepglobe	Average	FSS-1000	X-ray	Deepglobe	Average
PFENet (TPAMI2021) (Tian et al., 2020)	70.87	27.22	16.88	38.32	70.52	27.57	18.01	38.70
RePRI (CVPR2021) (Boudiaf et al., 2021)	70.96	65.08	25.03	53.69	74.23	65.48	27.41	55.71
HSNet (ICCV2021) (Min et al., 2021)	77.53	51.88	29.65	53.02	80.99	54.36	35.08	56.81
PATNet (ECCV2022) (Lei et al., 2022)	78.59	66.61	37.89	61.03	81.23	70.20	42.97	64.80
HDMNet (CVPR2023) (Peng et al., 2023)	75.10	30.60	25.40	43.70	78.60	31.30	39.10	49.67
RestNet (BMVC2023) (Huang et al., 2023)	81.50	70.40	22.70	58.20	<u>84.90</u>	73.70	29.90	62.83
PMNet (WACV2024) (Chen et al., 2024)	84.60	70.40	37.10	64.03	86.30	74.00	41.60	67.30
ABCDFSS (CVPR2024) (Herzog, 2024)	74.60	<u>79.80</u>	42.60	<u>65.67</u>	76.20	<u>81.40</u>	49.00	<u>68.87</u>
AgMTR (Ours)	<u>83.54</u>	86.50	<u>41.42</u>	70.49	84.36	88.85	<u>47.11</u>	73.44

utilized for training and testing are from different domains. Following the setup of ABCDFSS (Herzog, 2024) and PATNet (Lei et al., 2022), we evaluate the performance on three datasets with different domain shifts, including FSS-1000 (Li et al., 2020), Chest X-ray (Jaeger et al., 2014), and DeepGlobe (Demir et al., 2018), which cover 1,000 classes of everyday objects, X-ray images and 6 classes of satellite images, respectively. The proposed method is trained on

PASCAL VOC and evaluated on these three datasets, with the mIoU results and visualization results presented in Table 13 and Fig. 22. It can be found that our method achieves satisfactory performance, e.g., AgMTR exceeds ABCDFSS by 8.94% on FSS-1000, and by 6.7% on the Chest X-ray under the 1-shot setting. The above results demonstrate that even though our AgMTR is not specifically constructed for cross-domain scenarios, the designed local agents can dynam-

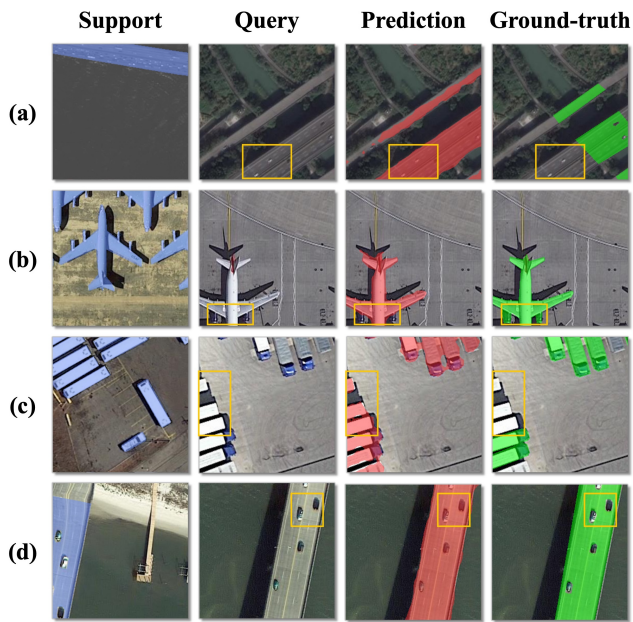


Fig. 23 Failure cases of the proposed method. From top to bottom: (a) the ‘Roadway’ on the land which is misinterpreted. (b) The ‘Engine’ in the shadow. (c) The similarity between ‘Large vehicles’ and ‘Containers’. (d) Overlap between ‘Vehicles’ and the ‘Bridge’.

ically mine class-specific semantics from labeled, unlabeled, and query images in the target domain to perform accurate segmentation and exhibit excellent generalisability.

5.6 Failure case analysis

By mining and optimizing local-aware agents from support, unlabeled, and query images, AgMTR is able to construct precise agent-level semantic correlation to efficiently perceive the interested object. However, it ignores the association between foreground objects and background, or other categories, producing several failure segmentation cases. Take the case (a) in Fig.23 as an example, the model fails to understand the ‘Bridge is always over water’ connection and incorrectly considers a ‘Road’ over the land as a ‘Bridge’. In addition, when the object appears in the shadow, the object shows extreme similarity with the background, or the object overlaps with other classes, the segmentation performance is also weak (see Fig.23.(b)-(d)). A potential solution to radically improve the FSS performance may be to utilize the diffusion models to generate more labeled images based on the support image to provide more robust guidance, such as DifFSS (Tan et al., 2023).

6 Conclusion

To correct the semantic ambiguity between the query FG and BG pixels due to pixel-level mismatch, this paper proposes a

novel Agent Mining Transformer (AgMTR) for remote sensing FSS, which can adaptively mine a set of representative agents to construct agent-level semantic correlation. Compared to pixel-level semantics, the agents are equipped with local contextual information and possess a broader receptive field, thus ensuring that the query pixels safely execute the semantic aggregation and enhancing the semantic clarity between the query FG and BG pixels. Experiment results on remote sensing scenarios iSAID and more common natural scenarios, i.e., PASCAL-5ⁱ and COCO-20ⁱ validate the effectiveness of the proposed AgMTR and set the state-of-the-art performance, which strongly demonstrates its generality and extensibility. In the future, we consider introducing the semantic information of linguistic modality in FSS tasks, such as Visual-Language models, and try to explore more challenging Zero-shot segmentation tasks.

Data Availability Statement

The datasets generated in this study are available from the iSAID¹ website, the PASCAL² website, and the MS COCO³ website.

Acknowledgments

This work was supported by the National Natural Science Foundation of China (NSFC) under Grant 62301538.

References

- Achanta R, Shaji A, Smith K, Lucchi A, Fua P, Süsstrunk S (2012) Slic superpixels compared to state-of-the-art superpixel methods. *IEEE transactions on pattern analysis and machine intelligence* 34(11):2274–2282
- Alajaji D, Alhichri HS, Ammour N, Alajlan N (2020) Few-shot learning for remote sensing scene classification. In: 2020 Mediterranean and Middle-East Geoscience and Remote Sensing Symposium (M2GARSS), IEEE, pp 81–84
- Bao X, Qin J, Sun S, Zheng Y, Wang X (2023) Relevant intrinsic feature enhancement network for few-shot semantic segmentation. *arXiv preprint arXiv:231206474*
- Bateni P, Goyal R, Masrani V, Wood F, Sigal L (2020) Improved few-shot visual classification. In: *Proceedings of the IEEE/CVF Conference on Computer Vision and Pattern Recognition*, pp 14493–14502
- Bi H, Feng Y, Yan Z, Mao Y, Diao W, Wang H, Sun X (2023) Not just learning from others but relying on yourself: A

¹ <https://captain-whu.github.io/iSAID/index>

² <http://host.robots.ox.ac.uk/pascal/VOC/>

³ <https://cocodataset.org/#home>

- new perspective on few-shot segmentation in remote sensing. *IEEE Transactions on Geoscience and Remote Sensing*
- Bi H, Feng Y, Diao W, Wang P, Mao Y, Fu K, Wang H, Sun X (2024) Prompt-and-transfer: Dynamic class-aware enhancement for few-shot segmentation. *IEEE Transactions on Pattern Analysis and Machine Intelligence*
- Boudiaf M, Kervadec H, Masud ZI, Piantanida P, Ben Ayed I, Dolz J (2021) Few-shot segmentation without meta-learning: A good transductive inference is all you need? In: *Proceedings of the IEEE/CVF conference on computer vision and pattern recognition*, pp 13979–13988
- Chen H, Dong Y, Lu Z, Yu Y, Han J (2024) Pixel matching network for cross-domain few-shot segmentation. In: *Proceedings of the IEEE/CVF Winter Conference on Applications of Computer Vision*, pp 978–987
- Chen LC, Papandreou G, Kokkinos I, Murphy K, Yuille AL (2014) Semantic image segmentation with deep convolutional nets and fully connected crfs. *arXiv preprint arXiv:14127062*
- Chen LC, Papandreou G, Kokkinos I, Murphy K, Yuille AL (2017) Deeplab: Semantic image segmentation with deep convolutional nets, atrous convolution, and fully connected crfs. *IEEE transactions on pattern analysis and machine intelligence* 40(4):834–848
- Chen Y, Liu Z, Xu H, Darrell T, Wang X (2021) Meta-baseline: Exploring simple meta-learning for few-shot learning. In: *Proceedings of the IEEE/CVF international conference on computer vision*, pp 9062–9071
- Cheng B, Misra I, Schwing AG, Kirillov A, Girdhar R (2022a) Masked-attention mask transformer for universal image segmentation. In: *Proceedings of the IEEE/CVF conference on computer vision and pattern recognition*, pp 1290–1299
- Cheng G, Cai L, Lang C, Yao X, Chen J, Guo L, Han J (2021) Spnet: Siamese-prototype network for few-shot remote sensing image scene classification. *IEEE Transactions on Geoscience and Remote Sensing* 60:1–11
- Cheng G, Lang C, Han J (2022b) Holistic prototype activation for few-shot segmentation. *IEEE Transactions on Pattern Analysis and Machine Intelligence* 45(4):4650–4666
- Csillik O (2017) Fast segmentation and classification of very high resolution remote sensing data using slic superpixels. *Remote Sensing* 9(3):243
- Cuturi M (2013) Sinkhorn distances: Lightspeed computation of optimal transport. *Advances in neural information processing systems* 26
- Demir I, Koperski K, Lindenbaum D, Pang G, Huang J, Basu S, Hughes F, Tuia D, Raskar R (2018) Deepglobe 2018: A challenge to parse the earth through satellite images. In: *Proc. IEEE Int. Conf. Comput. Vis. Pattern Recognit. Workshops*, pp 172–181
- Deng J, Dong W, Socher R, Li LJ, Li K, Fei-Fei L (2009) Imagenet: A large-scale hierarchical image database. In: *2009 IEEE conference on computer vision and pattern recognition*, Ieee, pp 248–255
- Dey V, Zhang Y, Zhong M (2010) A review on image segmentation techniques with remote sensing perspective, vol 38. na Vienna, Austria
- Diakogiannis FI, Waldner F, Caccetta P, Wu C (2020) Resunet-a: A deep learning framework for semantic segmentation of remotely sensed data. *ISPRS Journal of Photogrammetry and Remote Sensing* 162:94–114
- Dosovitskiy A, Beyer L, Kolesnikov A, Weissenborn D, Zhai X, Unterthiner T, Dehghani M, Minderer M, Heigold G, Gelly S, et al. (2020) An image is worth 16x16 words: Transformers for image recognition at scale. *arXiv preprint arXiv:201011929*
- Everingham M, Van Gool L, Williams CK, Winn J, Zisserman A (2010) The pascal visual object classes (voc) challenge. *International journal of computer vision* 88:303–338
- Feng Y, Diao W, Sun X, Li J, Chen K, Fu K, Gao X (2020) Npaloss: Neighboring pixel affinity loss for semantic segmentation in high-resolution aerial imagery. *ISPRS Annals of the Photogrammetry, Remote Sensing and Spatial Information Sciences* 2:475–482
- Feng Y, Sun X, Diao W, Li J, Gao X (2021) Double similarity distillation for semantic image segmentation. *IEEE Transactions on Image Processing* 30:5363–5376
- Finn C, Abbeel P, Levine S (2017) Model-agnostic meta-learning for fast adaptation of deep networks. In: *International conference on machine learning*, PMLR, pp 1126–1135
- Hariharan B, Arbeláez P, Girshick R, Malik J (2014) Simultaneous detection and segmentation. In: *Computer Vision—ECCV 2014: 13th European Conference, Zurich, Switzerland, September 6–12, 2014, Proceedings, Part VII* 13, Springer, pp 297–312
- He K, Zhang X, Ren S, Sun J (2016) Identity mappings in deep residual networks. In: *Computer Vision—ECCV 2016: 14th European Conference, Amsterdam, The Netherlands, October 11–14, 2016, Proceedings, Part IV* 14, Springer, pp 630–645
- He S, Ding H, Jiang W (2023a) Primitive generation and semantic-related alignment for universal zero-shot segmentation. In: *Proceedings of the IEEE/CVF Conference on Computer Vision and Pattern Recognition*, pp 11238–11247
- He S, Ding H, Jiang W (2023b) Semantic-promoted debiasing and background disambiguation for zero-shot instance segmentation. In: *Proceedings of the IEEE/CVF Conference on Computer Vision and Pattern Recognition*, pp 19498–19507

- He S, Ding H, Jiang X, Wen B (2024) Segpoint: Segment any point cloud via large language model. arXiv preprint arXiv:240713761
- Herzog J (2024) Adapt before comparison: A new perspective on cross-domain few-shot segmentation. In: Proceedings of the IEEE/CVF Conference on Computer Vision and Pattern Recognition, pp 23605–23615
- Hu Z, Sun Y, Yang Y (2022) Suppressing the heterogeneity: A strong feature extractor for few-shot segmentation. In: The Eleventh International Conference on Learning Representations
- Huang X, Zhu C, Chen W (2023) Restnet: Boosting cross-domain few-shot segmentation with residual transformation network. arXiv preprint arXiv:230813469
- Jaeger S, Candemir S, Antani S, Wang YXJ, Lu PX, Thoma G (2014) Two public chest x-ray datasets for computer-aided screening of pulmonary diseases. *Quantitative imaging in medicine and surgery* 4(6):475
- Jamal MA, Qi GJ (2019) Task agnostic meta-learning for few-shot learning. In: Proceedings of the IEEE/CVF Conference on Computer Vision and Pattern Recognition, pp 11719–11727
- Jiang X, Zhou N, Li X (2022) Few-shot segmentation of remote sensing images using deep metric learning. *IEEE Geoscience and Remote Sensing Letters* 19:1–5
- Kim J, Chi M (2021) Saffnet: Self-attention-based feature fusion network for remote sensing few-shot scene classification. *Remote Sensing* 13(13):2532
- Kotaridis I, Lazaridou M (2021) Remote sensing image segmentation advances: A meta-analysis. *ISPRS Journal of Photogrammetry and Remote Sensing* 173:309–322
- Lang C, Cheng G, Tu B, Han J (2022a) Learning what not to segment: A new perspective on few-shot segmentation. In: Proceedings of the IEEE/CVF conference on computer vision and pattern recognition, pp 8057–8067
- Lang C, Tu B, Cheng G, Han J (2022b) Beyond the prototype: Divide-and-conquer proxies for few-shot segmentation. arXiv preprint arXiv:220409903
- Lang C, Cheng G, Tu B, Han J (2023a) Global rectification and decoupled registration for few-shot segmentation in remote sensing imagery. *IEEE Transactions on Geoscience and Remote Sensing* 61:1–11, DOI 10.1109/TGRS.2023.3301003
- Lang C, Cheng G, Tu B, Han J (2023b) Global rectification and decoupled registration for few-shot segmentation in remote sensing imagery. *IEEE Transactions on Geoscience and Remote Sensing*
- Lang C, Cheng G, Tu B, Li C, Han J (2023c) Base and meta: A new perspective on few-shot segmentation. *IEEE Transactions on Pattern Analysis and Machine Intelligence*
- Lang C, Cheng G, Tu B, Li C, Han J (2023d) Retain and recover: Delving into information loss for few-shot segmentation. *IEEE Transactions on Image Processing* 32:5353–5365, DOI 10.1109/TIP.2023.3315555
- Lang C, Wang J, Cheng G, Tu B, Han J (2023e) Progressive parsing and commonality distillation for few-shot remote sensing segmentation. *IEEE Transactions on Geoscience and Remote Sensing* 61:1–10, DOI 10.1109/TGRS.2023.3286183
- Lang C, Cheng G, Tu B, Han J (2024) Few-shot segmentation via divide-and-conquer proxies. *International Journal of Computer Vision* 132(1):261–283
- Lei S, Zhang X, He J, Chen F, Du B, Lu CT (2022) Cross-domain few-shot semantic segmentation. In: European Conference on Computer Vision, Springer, pp 73–90
- Li G, Jampani V, Sevilla-Lara L, Sun D, Kim J, Kim J (2021) Adaptive prototype learning and allocation for few-shot segmentation. In: Proceedings of the IEEE/CVF conference on computer vision and pattern recognition, pp 8334–8343
- Li X, Wei T, Chen YP, Tai YW, Tang CK (2020) Fss-1000: A 1000-class dataset for few-shot segmentation. In: Proc. IEEE Int. Conf. Comput. Vis. Pattern Recognit., pp 2869–2878
- Li Z, Zhou F, Chen F, Li H (2017) Meta-sgd: Learning to learn quickly for few-shot learning. arXiv preprint arXiv:170709835
- Lian R, Huang L (2021) Weakly supervised road segmentation in high-resolution remote sensing images using point annotations. *IEEE Transactions on Geoscience and Remote Sensing* 60:1–13
- Lin TY, Maire M, Belongie S, Hays J, Perona P, Ramanan D, Dollár P, Zitnick CL (2014) Microsoft coco: Common objects in context. In: Computer Vision–ECCV 2014: 13th European Conference, Zurich, Switzerland, September 6–12, 2014, Proceedings, Part V 13, Springer, pp 740–755
- Liu W, Zhang C, Lin G, Liu F (2020a) Crnet: Cross-reference networks for few-shot segmentation. In: Proceedings of the IEEE/CVF Conference on Computer Vision and Pattern Recognition, pp 4165–4173
- Liu Y, Zhang X, Zhang S, He X (2020b) Part-aware prototype network for few-shot semantic segmentation. In: Computer Vision–ECCV 2020: 16th European Conference, Glasgow, UK, August 23–28, 2020, Proceedings, Part IX 16, Springer, pp 142–158
- Liu Y, Liu N, Cao Q, Yao X, Han J, Shao L (2022a) Learning non-target knowledge for few-shot semantic segmentation. In: Proceedings of the IEEE/CVF Conference on Computer Vision and Pattern Recognition, pp 11573–11582
- Liu Y, Liu N, Yao X, Han J (2022b) Intermediate prototype mining transformer for few-shot semantic segmentation. *Advances in Neural Information Processing Systems* 35:38020–38031
- Long J, Shelhamer E, Darrell T (2015) Fully convolutional networks for semantic segmentation. In: Proceedings of the IEEE conference on computer vision and pattern recog-

- dition, pp 3431–3440
- Mao Y, Chen K, Diao W, Sun X, Lu X, Fu K, Weinmann M (2022a) Beyond single receptive field: A receptive field fusion-and-stratification network for airborne laser scanning point cloud classification. *ISPRS Journal of Photogrammetry and Remote Sensing* 188:45–61
- Mao Y, Guo Z, Xiaonan L, Yuan Z, Guo H (2022b) Bidirectional feature globalization for few-shot semantic segmentation of 3d point cloud scenes. In: 2022 International Conference on 3D Vision (3DV), IEEE, pp 505–514
- Mao Y, Chen K, Zhao L, Chen W, Tang D, Liu W, Wang Z, Diao W, Sun X, Fu K (2023) Elevation estimation-driven building 3-d reconstruction from single-view remote sensing imagery. *IEEE Transactions on Geoscience and Remote Sensing* 61:1–18
- Mao YQ, Bi H, Xu L, Chen K, Wang Z, Sun X, Fu K (2024) Sdl-mvs: View space and depth deformable learning paradigm for multi-view stereo reconstruction in remote sensing. arXiv preprint arXiv:240517140
- Min J, Kang D, Cho M (2021) Hypercorrelation squeeze for few-shot segmentation. In: Proceedings of the IEEE/CVF international conference on computer vision, pp 6941–6952
- Nguyen K, Todorovic S (2019) Feature weighting and boosting for few-shot segmentation. In: Proceedings of the IEEE/CVF International Conference on Computer Vision, pp 622–631
- Niu R, Sun X, Tian Y, Diao W, Feng Y, Fu K (2022) Improving semantic segmentation in aerial imagery via graph reasoning and disentangled learning. *IEEE Transactions on Geoscience and Remote Sensing* 60:1–18, DOI 10.1109/TGRS.2021.3121471
- Paszke A, Gross S, Massa F, Lerer A, Bradbury J, Chanan G, Killeen T, Lin Z, Gimelshein N, Antiga L, et al. (2019) Pytorch: An imperative style, high-performance deep learning library. *Advances in neural information processing systems* 32
- Peng B, Tian Z, Wu X, Wang C, Liu S, Su J, Jia J (2023) Hierarchical dense correlation distillation for few-shot segmentation. In: Proceedings of the IEEE/CVF Conference on Computer Vision and Pattern Recognition, pp 23641–23651
- Peng C, Zhang K, Ma Y, Ma J (2021) Cross fusion net: A fast semantic segmentation network for small-scale semantic information capturing in aerial scenes. *IEEE Transactions on Geoscience and Remote Sensing* 60:1–13
- Ravi S, Larochelle H (2016) Optimization as a model for few-shot learning. In: International conference on learning representations
- Ronneberger O, Fischer P, Brox T (2015) U-net: Convolutional networks for biomedical image segmentation. In: Medical Image Computing and Computer-Assisted Intervention–MICCAI 2015: 18th International Conference, Munich, Germany, October 5–9, 2015, Proceedings, Part III 18, Springer, pp 234–241
- Schmitt M, Prexl J, Ebel P, Liebel L, Zhu XX (2020) Weakly supervised semantic segmentation of satellite images for land cover mapping—challenges and opportunities. arXiv preprint arXiv:200208254
- Shaban A, Bansal S, Liu Z, Essa I, Boots B (2017) One-shot learning for semantic segmentation. arXiv preprint arXiv:170903410
- Snell J, Swersky K, Zemel R (2017) Prototypical networks for few-shot learning. *Advances in neural information processing systems* 30
- Sun Q, Liu Y, Chua TS, Schiele B (2019) Meta-transfer learning for few-shot learning. In: Proceedings of the IEEE/CVF conference on computer vision and pattern recognition, pp 403–412
- Sun X, Shi A, Huang H, Mayer H (2020) Bas4net: Boundary-aware semi-supervised semantic segmentation network for very high resolution remote sensing images. *IEEE Journal of Selected Topics in Applied Earth Observations and Remote Sensing* 13:5398–5413
- Sun X, Yan Q, Deng C, Liu C, Jiang Y, Hou Z, Lu W, Yao F, Liu X, Hao L, et al. (2024) Recon1m: A large-scale benchmark dataset for relation comprehension in remote sensing imagery. arXiv preprint arXiv:240606028
- Sung F, Yang Y, Zhang L, Xiang T, Torr PH, Hospedales TM (2018) Learning to compare: Relation network for few-shot learning. In: Proceedings of the IEEE conference on computer vision and pattern recognition, pp 1199–1208
- Tan W, Chen S, Yan B (2023) Diffss: Diffusion model for few-shot semantic segmentation. arXiv preprint arXiv:230700773
- Tian Z, Zhao H, Shu M, Yang Z, Li R, Jia J (2020) Prior guided feature enrichment network for few-shot segmentation. *IEEE transactions on pattern analysis and machine intelligence* 44(2):1050–1065
- Tian Z, Zhao H, Shu M, Yang Z, Li R, Jia J (2022) Prior guided feature enrichment network for few-shot segmentation. *IEEE Transactions on Pattern Analysis & Machine Intelligence* 44(02):1050–1065
- Touvron H, Cord M, Douze M, Massa F, Sablayrolles A, Jégou H (2021) Training data-efficient image transformers & distillation through attention. In: International conference on machine learning, PMLR, pp 10347–10357
- Veličković P, Cucurull G, Casanova A, Romero A, Lio P, Bengio Y (2017) Graph attention networks. arXiv preprint arXiv:171010903
- Vinyals O, Blundell C, Lillicrap T, Wierstra D, et al. (2016) Matching networks for one shot learning. *Advances in neural information processing systems* 29
- Wang B, Wang Z, Sun X, Wang H, Fu K (2021) Dmml-net: Deep metametric learning for few-shot geographic object segmentation in remote sensing imagery. *IEEE Transac-*

- tions on Geoscience and Remote Sensing 60:1–18
- Wang D, Zhang J, Du B, Xia GS, Tao D (2022a) An empirical study of remote sensing pretraining. *IEEE Transactions on Geoscience and Remote Sensing* 61:1–20
- Wang J, HQ Ding C, Chen S, He C, Luo B (2020a) Semi-supervised remote sensing image semantic segmentation via consistency regularization and average update of pseudo-label. *Remote Sensing* 12(21):3603
- Wang JX, Chen SB, Ding CH, Tang J, Luo B (2022b) Semi-supervised semantic segmentation of remote sensing images with iterative contrastive network. *IEEE Geoscience and Remote Sensing Letters* 19:1–5
- Wang K, Liew JH, Zou Y, Zhou D, Feng J (2019) Panet: Few-shot image semantic segmentation with prototype alignment. In: proceedings of the IEEE/CVF international conference on computer vision, pp 9197–9206
- Wang S, Chen W, Xie SM, Azzari G, Lobell DB (2020b) Weakly supervised deep learning for segmentation of remote sensing imagery. *Remote Sensing* 12(2):207
- Wang Y, Yao Q, Kwok JT, Ni LM (2020c) Generalizing from a few examples: A survey on few-shot learning. *ACM computing surveys (csur)* 53(3):1–34
- Wang Y, Albrecht CM, Braham NAA, Mou L, Zhu XX (2022c) Self-supervised learning in remote sensing: A review. *IEEE Geoscience and Remote Sensing Magazine* 10(4):213–247
- Wang Y, Sun R, Zhang Z, Zhang T (2022d) Adaptive agent transformer for few-shot segmentation. In: *European Conference on Computer Vision*, Springer, pp 36–52
- Wang Y, Luo N, Zhang T (2024) Focus on query: Adversarial mining transformer for few-shot segmentation. *Advances in Neural Information Processing Systems* 36
- Waqas Zamir S, Arora A, Gupta A, Khan S, Sun G, Shahbaz Khan F, Zhu F, Shao L, Xia GS, Bai X (2019) isaid: A large-scale dataset for instance segmentation in aerial images. In: *Proceedings of the IEEE/CVF Conference on Computer Vision and Pattern Recognition Workshops*, pp 28–37
- Xu L, Lu W, Yu H, Mao Y, Bi H, Liu C, Sun X, Fu K (2024a) Taformer: A unified target-aware transformer for video and motion joint prediction in aerial scenes. *IEEE Transactions on Geoscience and Remote Sensing*
- Xu Q, Zhao W, Lin G, Long C (2023) Self-calibrated cross attention network for few-shot segmentation. In: *Proceedings of the IEEE/CVF International Conference on Computer Vision*, pp 655–665
- Xu Y, Bi H, Yu H, Lu W, Li P, Li X, Sun X (2024b) Attention-based contrastive learning for few-shot remote sensing image classification. *IEEE Transactions on Geoscience and Remote Sensing*
- Yang B, Liu C, Li B, Jiao J, Ye Q (2020a) Prototype mixture models for few-shot semantic segmentation. In: *Computer Vision–ECCV 2020: 16th European Conference, Glasgow, UK, August 23–28, 2020, Proceedings, Part VIII* 16, Springer, pp 763–778
- Yang X, Wang B, Chen K, Zhou X, Yi S, Ouyang W, Zhou L (2020b) Brinet: Towards bridging the intra-class and inter-class gaps in one-shot segmentation. *arXiv preprint arXiv:200806226*
- Yang Y, Chen Q, Feng Y, Huang T (2023) Mianet: Aggregating unbiased instance and general information for few-shot semantic segmentation. In: *Proceedings of the IEEE/CVF Conference on Computer Vision and Pattern Recognition*, pp 7131–7140
- Yao X, Cao Q, Feng X, Cheng G, Han J (2021) Scale-aware detailed matching for few-shot aerial image semantic segmentation. *IEEE Transactions on Geoscience and Remote Sensing* 60:1–11
- Ye HJ, Hu H, Zhan DC, Sha F (2020) Few-shot learning via embedding adaptation with set-to-set functions. In: *Proceedings of the IEEE/CVF conference on computer vision and pattern recognition*, pp 8808–8817
- Yuan X, Shi J, Gu L (2021) A review of deep learning methods for semantic segmentation of remote sensing imagery. *Expert Systems with Applications* 169:114417
- Zeng Q, Geng J (2022) Task-specific contrastive learning for few-shot remote sensing image scene classification. *ISPRS Journal of Photogrammetry and Remote Sensing* 191:143–154
- Zhang B, Xiao J, Qin T (2021a) Self-guided and cross-guided learning for few-shot segmentation. In: *Proceedings of the IEEE/CVF Conference on Computer Vision and Pattern Recognition*, pp 8312–8321
- Zhang B, Zhang Y, Li Y, Wan Y, Guo H, Zheng Z, Yang K (2022a) Semi-supervised deep learning via transformation consistency regularization for remote sensing image semantic segmentation. *IEEE Journal of Selected Topics in Applied Earth Observations and Remote Sensing*
- Zhang C, Lin G, Liu F, Yao R, Shen C (2019) Canet: Class-agnostic segmentation networks with iterative refinement and attentive few-shot learning. In: *Proceedings of the IEEE/CVF conference on computer vision and pattern recognition*, pp 5217–5226
- Zhang C, Cai Y, Lin G, Shen C (2022b) Deepemd: Differentiable earth mover’s distance for few-shot learning. *IEEE Transactions on Pattern Analysis and Machine Intelligence* 45(5):5632–5648
- Zhang G, Kang G, Yang Y, Wei Y (2021b) Few-shot segmentation via cycle-consistent transformer. *Advances in Neural Information Processing Systems* 34:21984–21996
- Zhang JW, Sun Y, Yang Y, Chen W (2022c) Feature-proxy transformer for few-shot segmentation. *Advances in Neural Information Processing Systems* 35:6575–6588
- Zhang L, Zhang L (2022) Artificial intelligence for remote sensing data analysis: A review of challenges and opportunities. *IEEE Geoscience and Remote Sensing Magazine*

10(2):270–294

- Zhao H, Shi J, Qi X, Wang X, Jia J (2017) Pyramid scene parsing network. In: Proceedings of the IEEE conference on computer vision and pattern recognition, pp 2881–2890
- Zhong Q, Chen L, Qian Y (2020) Few-shot learning for remote sensing image retrieval with maml. In: 2020 IEEE International Conference on Image Processing (ICIP), IEEE, pp 2446–2450
- Zhu J, Yang K, Guan N, Yi X, Qiu C (2023) Hcpnet: Learning discriminative prototypes for few-shot remote sensing image scene classification. *International Journal of Applied Earth Observation and Geoinformation* 123:103447